REVISED VERSION 12 July 2019

Radio occultation observations of the solar corona over 1.60-1.86$R_\odot$: Faraday rotation and frequency-shift analysis

David. B. Wexler[1*], Joseph V. Hollweg[2], Anatoli I. Efimov[3], Paul Song[4], Elizabeth A. Jensen[5], Roberto Lionello[6], Juha Vierinen[7], Anthea J. Coster[8]

[1]University of Southern Queensland, Centre for Astrophysics, Toowoomba, AU
[2]Department of Physics, University of New Hampshire, Durham, NH, USA
[3]Kotel'nikov Institute of Radio Engineering and Electronics, Fryazino Branch, Russian Academy of Sciences, 141190, Fryazino, RU
[4]Department of Physics, University of Massachusetts Lowell, Lowell, MA, USA
[5]Planetary Science Institute, Tuscon, AZ, USA
[6]Predictive Science, Inc., San Diego, CA, USA
[7]Department of Physics and Technology, University of Tromsø, Tromsø, Norway
[8]MIT Haystack Observatory, Westford, MA, USA

.

Key Points:

- Transcoronal Faraday rotation and radio frequency measurements constrain mid-coronal electron number densities and magnetic field strengths
- MHD coronal models provide detailed magnetic field solutions that facilitate interpretation of Faraday rotation observations
- The low-heliolatitude mid-corona includes regions characterized by relatively low Alfvén wave speeds and non-radial magnetic fields

This article has been accepted for publication and undergone full peer review but has not been through the copyediting, typesetting, pagination and proofreading process which may lead to differences between this version and the Version of Record. Please cite this article as doi: 10.1029/2019JA026937

*Guest research student, MIT Haystack Observatory, Westford, MA, USA

Corresponding author: David B. Wexler, dwexler@mit.edu, David.Wexler@usq.edu.au

Abstract

The study of coronal energy transport, central to the solar wind acceleration problem, relies upon accurate representation of magnetic fields and plasma electron densities. This information is difficult to obtain in mid-to-lower coronal regions that may contain complex magnetic structures. Faraday rotation (FR) solar radio occultation observations, which reveal line-of-sight (LOS) integrated product of the coronal magnetic field and electron density, can help characterize the coronal environment and constrain magnetic field strengths. Global magnetohydrodynamic (MHD) models use specified synoptic solar surface magnetograms and may be used to facilitate FR interpretation by estimating detailed magnetic field properties along the radio LOS. We present a hybrid FR analysis incorporating magnetic field solutions from an MHD coronal model, and an electron density radial profile conforming to radio frequency shift observations. The FR modeled by the hybrid method is compared to MESSENGER spacecraft radio FR observations through a coronal region of low heliolatitudes, and radial distance 1.60-1.86$R_\odot$ from the heliocenter, collected during a state of relative solar quiescence. The hybrid model resonably reproduces the form, polarity and magnitude of the observed FR. For this specific coronal region, the calculated radial profile of electron concentrations and varied magnetic field strengths indicate Alfvén wave speeds below 50 km/s close to the point of closest approach but near 400 km/s in adjacent regions along the sounding LOS. The new approach of combining MHD models with radio sounding observations supports study of MHD wave processes in the challenging mid-coronal magneto-ionic environment.

1 Introduction

Data-driven characterization of the Sun's magnetic fields is requisite for progress in the study of coronal energy transport and solar wind acceleration. During solar minimum, the solar corona is organized into a globally dipolar magnetic configuration, with polar regions typically exhibiting low-density, open-field structures associated with the fast solar winds, and equatorial plasma organized into nearly radial, high-density streamer formations that are associated with the slow solar winds (Woch et al., 1997). The streamers are organized over closed magnetic fields, complicating the analysis of slow solar wind formation (Abbo et al., 2016; Brooks et al., 2015).

Slow solar winds begin substantial acceleration above heliocentric radial distance (in solar radius units, $R_\odot$) $\sim 2.5R_\odot$ (Sheeley et al., 1997). The acceleration continues out into the extended corona and heliosphere (Efimov et al., 2018). Magnetohydrodynamic (MHD) waves are believed to play an important role in energy transformation and transport for this process. While there is little doubt that the MHD waves are present throughout all levels of the solar atmosphere and corona, an integrated picture that explains the solar wind acceleration and links the findings from different solar altitudes remains elusive (Cranmer et al., 2015). Arregui (2015) suggests that future observations "should concentrate on tracking the flow of energy across different regions of the atmosphere". Such a mapping of MHD wave energy through the inner corona to the slow solar wind acceleration zone hinges on proper characterization of the magnetic fields and electron densities.

Although the nomenclature has not yet been standardized, here we define the low-heliolatitude middle corona as the magnetized-plasma environment between 1.4-2.5$R_\odot$ above the heliocenter, similar to conventions and terminology used by e.g. Badalyan (1996); Koutchmy (2004); Mancuso et al. (2003); Mancuso and Garzelli (2013a). We refer to the region below $1.4R_\odot$ as the lower corona, which extends down to the base of corona adjacent to the transition region, around 2 Mm above the photospheric surface. Using this definition, magnetic fields of the lower corona are amenable to evaluation by extreme ultraviolet (EUV) imaging, e.g. (Verwichte et al., 2009; Ofman & Wang, 2008). In contrast, indirect measurements remain the main option to obtain crucial magnetic field information in the middle corona, where the field structures are often complex and in transition towards

streamer organization. These indirect measurements must be interpreted in model-specific contexts.

Techniques to analyze solar eruptions in the proximity of active regions have been developed to obtain magnetic field strength in the low- to mid-corona (Mancuso et al., 2019; Mancuso & Garzelli, 2013a; Gopalswamy et al., 2012; Mancuso et al., 2003). Solar outburst radio analysis was derived from a method developed for analysis of the bow shock of the terrestrial magnetosphere, applied in a novel manner to the case of a CME emerging into a background coronal field (Mancuso et al., 2019). The technique provided important information in the heliocentric radial distance range 1.2-1.5$R_\odot$ (Gopalswamy et al., 2012) using SDO imaging of CME ejections and the associated type II radio bursts. Mancuso et al. (2003) probed the 1.5-2.3$R_\odot$ mid-coronal region by analysis of type II radio bursts. Since the solar eruption events provide the basis for the method, it is important to note that the results selectively apply to active coronal states with propensity for outburst, while excluding steady quiescent Sun coronal conditions.

Faraday rotation (FR) analysis has been used to investigate coronal magnetic fields using natural and celestial radio sources (Pätzold et al., 1987; Ingleby et al., 2007; Mancuso & Garzelli, 2013b, 2013c; Le Chat et al., 2014; Jensen, Bisi, et al., 2013; Kooi et al., 2014). FR is the change in polarization position angle, $\Delta\chi$, that occurs when electromagnetic radiation containing a linearly polarized component traverses a magnetized plasma. Rotation of $\Delta\chi$ occurs in accordance with the integrated product of electron number density (n_e) and component of the magnetic field aligned with the radio ray path (hereafter, line-of-sight, LOS) from transmitting spacecraft to the terrestrial receiving radio telescope:

$$\Delta\chi = \xi \int_{SC}^{\oplus} n_e \vec{B} \cdot d\vec{S} \tag{1}$$

where $d\vec{S}$ is the path increment along the LOS from the spacecraft (SC) to Earth ($\oplus$) and $\vec{B}$ is the magnetic field vector at that location and

$$\xi = \frac{1}{f_0^2} \frac{e^3}{8\pi^2 \epsilon_0 m_e^2 c} \tag{2}$$

with radio transmission frequency f_0, electron mass m_e, electric charge e, vacuum permeability ϵ_0 and vacuum speed of light c. S.I. units are adopted throughout this work unless otherwise noted. For X-band 8.4 GHz radio transmissions studied in the present work, the constants consolidate to $\xi = 3.35 \times 10^{-16}$ rad T^{-1} m^2.

Although the FR techniques are limited by LOS integration, the effects producing the radio signal disturbances are usually greatest near the point of closest solar approach. The point of closest solar approach on the sounding LOS is also referred to as the proximate point, and the heliocentric distance to this point is called the solar offset, SO, typically given in $R_\odot$ units. Summaries of prior coronal FR research can be found in Bird (1982, 2007); Efimov et al. (2015), also see (Kooi et al., 2014; Kooi, 2016). Almost all the data for these studies were obtained at SO >3$R_\odot$, where the open field lines structures dominate and simplifying assumptions about the field may be introduced. Radial magnetic fields alone tend to cancel LOS-aligned field components by symmetry with respect to the LOS proximate point, and produce very little net FR when integrated on the LOS. Observable FR therefore is dominated by asymmetric magnetic fields and/or electron densities. Previous studies introduced the magnetic field asymmetry as an estimated single polarity-reversal sector boundary on an otherwise radial field, and interpreted the data on that basis. However, the results do not necessarily extrapolate to the deeper, low-to-middle coronal regions due to the changing power law relationships of electron density and departure from radial magnetic field structuring. Until now, detailed magnetic field analysis in the middle corona using FR has been lacking.

We had an opportunity to analyze radio occultation observations of the equatorial corona at close SO near solar minimum, using X-band radio transmissions of the MES-

SENGER (MErcury Surface, Space ENvironment, GEochemistry and Ranging) spacecraft during egress from solar conjunction in November 2009. An initial report on these MESSENGER 2009 spacecraft transcoronal FR observations below SO $2R_\odot$ characterized the FR but did not isolate magnetic field strengths (Jensen, Bisi, et al., 2013). Subsequent reports on the same observations analyzed FR fluctuations (Jensen, Nolan, et al., 2013; Wexler et al., 2017) using modeled magnetic field strengths from the literature. We now present a further investigation of the MESSENGER 10 Nov 2009 radio occultation observations, with emphasis the magnetic field. Since the problems of asymmetric and non-radial magnetic field features confound analysis of FR using the conventional power-law models, we undertook a mid-corona FR analysis supported by an MHD 3-D coronal model. The MHD model solutions provide the estimated magnetic field vectors along each LOS analyzed, specific to the Carrington rotation (CR) under study. In addition, Doppler-corrected frequency-shift analysis data (Dolbezhev et al., 1986; Efimov et al., 1990) are used to refine power-law expressions of coronal electron density. Using frequency shift results and the MHD model magnetic field solutions, we establish a fairly good correlation between the FR observations and the modeled FR.

Our report is organized as follows. The MESSENGER observations and data processing are addressed in §2. The MHD model, data mapping and LOS magnetic field information are presented in §3. In §4 we discuss electron number density models and show the radio frequency shift method that improves the electron density model for a given study interval and location. A comparison between observed Faraday rotation and a hybrid FR analysis based on the MHD model together with improved number density modeling are given in §5. The conclusions are summarized in §6.

2 Transcoronal radio observations

2.1 MESSENGER spacecraft recordings

We obtained 4 hours of near-continuous recording of MESSENGER spacecraft X-band (8.4 GHz) radio transmissions during egress from solar conjunction on 10 Nov 2009. The Sun was still in a fairly quiet state of activity following the deep solar minimum of solar cycle 23. The MESSENGER spacecraft was on a Mercury flyby trajectory, positioned in near-equatorial coronal occultation with closest heliocentric approach to the LOS ranging from $1.605R_\odot$ to $1.864R_\odot$ during the observations.

The MESSENGER X-band down-link signal is transmitted in mostly right-circular polarization (RCP). A non-unitary axial ratio in the transmitter circular polarization results in a small representation of left-circular polarization (LCP) signal, resulting in a linear polarization component of several percent. The plane of polarization, and FR, can be recovered from the RCP and LCP observations (Jensen et al., 2005; Wexler et al., 2017). FR may be understood by considering the linearly polarized radio signal as being composed of left- and right-circularly polarized components (RCP, LCP). The refractive index of a radio wave propagating in a magnetized plasma depends on the wave frequency, f_0, the electron number density, n_e, and the magnetic field intensity in the direction of wave propagation (Bastian, 2001; Bird, 2007; Mancuso & Garzelli, 2013b). In the presence of a magnetized plasma, the LCP propagates with a higher phase velocity than RCP, resulting in a net rotation of the polarization position angle.

The observations were recorded in dual-feed circular polarization channels using the NRAO Green Bank 100-m radio telescope. RCP and LCP channels were down-converted by a heterodyne system to a baseband frequency. For each channel of polarization, the quadrature-phased I(real) and Q(imaginary) signal components were recorded as complex numbers at a sampling rate of 5MHz. Further details on this set of observations may be found in Jensen, Bisi, et al. (2013); Wexler et al. (2017).

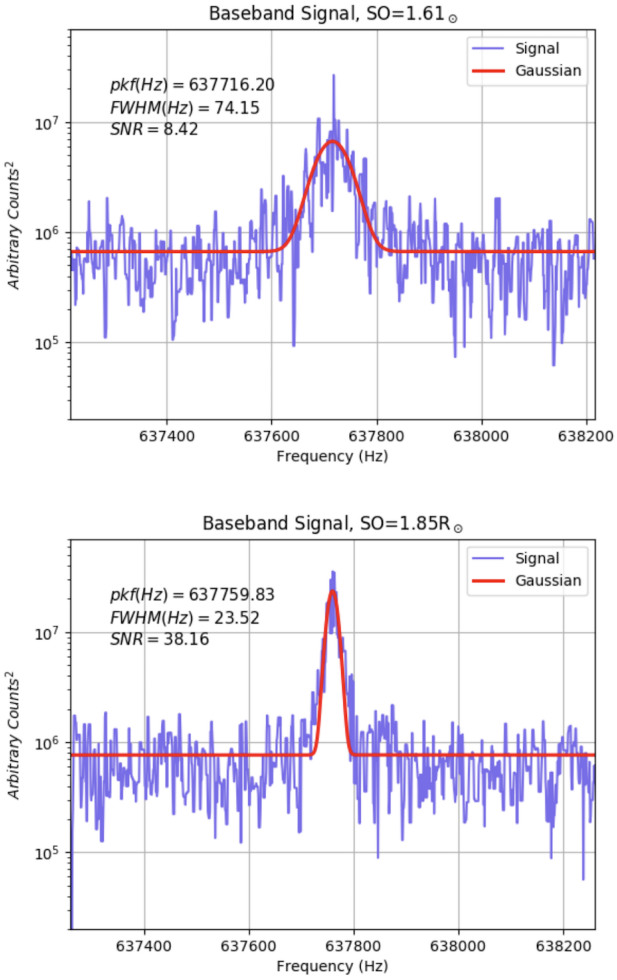

Figure 1. Gaussian fit to spectrogram of right circular polarization signal intensity for a one-second data frame. The signal is broadened at this coronal depth due to time-varying density inhomogeneities in the corona. Above: solar offset 1.61R$_\odot$. Below: solar offset 1.85R$_\odot$. FHWM = full width at half maximum amplitude, the measure of spectral broadening; pkf = fitted peak signal frequency; SNR = signal-to-noise ratio.

2.2 Signal processing

The RCP and LCP signals were reconstituted from the quadrature components and analyzed in sequential one-second segments. The radio signal was broadened in frequency due to turbulent density fluctuations. In each one-second data frame, the center frequency was obtained by best fit of a Gaussian distribution to the spectrogram of signal intensity (Figure 1). Spectral broadening is evident, with the Full-Width Half-Maximum (FWHM) measure being about three times higher at SO=1.61R$_\odot$ than the value at 1.85R$_\odot$. Spectral broadening is related to rate and intensity of density inhomogeneities crossing the LOS, and is thus dependent on electron density, plasma radial outflow speed and the spectral characteristics of the coronal turbulence (Bird, 1982; Woo et al., 1976). It is likely that the increased FWHM noted at the closer SO is related to increased electron density, although countereffects of increasing flow speed and turbulence may blunt the range of FWHM observed.

In the frequency domain, the RCP signal is designated in the complex spectrum as Z_R and that of LCP is Z_L. Power products were calculated as $\langle Z_R Z_R^* \rangle$, $\langle Z_L Z_L^* \rangle$ and cross-spectrum $\langle Z_R Z_L^* \rangle$, where the asterisk denotes complex conjugate. From these the Stokes parameters I, Q, U and V were calculated. Stokes I is the total intensity, $\langle Z_R Z_R^* \rangle + \langle Z_L Z_L^* \rangle$. Stokes V is the circular polarization intensity, $\langle Z_R Z_R^* \rangle - \langle Z_L Z_L^* \rangle$. In this data the mean fractional circular polarization was 0.95, with the remainder of power being in the linearly polarized components needed to asses FR. Stokes Q and U are obtained from the real and imaginary parts of the cross-spectrum; $Q = 2\mathrm{Re}\langle Z_L^* Z_R \rangle$ and $U = -2\mathrm{Im}\langle Z_L^* Z_R \rangle$. For each sequential one-second analysis frame, the polarization position angle was calculated as

$$\chi = \frac{1}{2} \arctan \frac{U}{Q}. \tag{3}$$

The polarization position angle has intrinsic $\pm n\pi$ uncertainty. The position angle turnover, which would normally reset the angular measure to zero beyond π radians, was removed by a computational unwrapping routine to allow a continuous curve of the cumulative angular turn. The absolute offset of this cumulative or running position angle was unknown, and initially was set to zero radians at the end of FR curve. The parallactic angle correction for the position of the LOS in the plane of the sky was applied to yield the final FR curve.

2.3 Observational data

The observed time series of polarization position angle, whose progression demonstrates the Faraday rotation, is shown in §5 with analysis results, and was reported previously (Wexler et al., 2017). Over the 4-hours of observations, the polarization position angle trends lower by 7.24 radians. The FR absolute offset is initially unknown; a suitable FR offset will be proposed later in the report, when the FR integral is computed using the model data.

We define positive FR as counterclockwise rotation of the position angle as viewed from the Earth when a magnetic field component points towards the terrestrial observer. Thus we are defining a positive magnetic field component on the LOS as being towards the observer; this is different than the typical physics convention of a positive magnetic field vector pointing away from the source. In our case, such an outgoing magnetic field vector from the Sun may project on the sounding LOS to produce either positive (towards Earth) of negative (away from Earth) LOS component (hereafter denoted $B_{||}$) by our convention. For an idealized radially symmetric coronal magnetic field, the positive B components on one side of the proximate point would cancel those of the other side and the net observed FR would be zero. Thus, if the electron density is assumed radially symmetric, concordance with our FR observations requires asymmetric magnetic fields across the proximate point, with a net LOS decreasing positive $B_{||}$ or an increasing negative $B_{||}$ as defined above.

Time variations and irregular oscillatory behavior of the FR pattern are also noted. These FR fluctuations are of interest in the study of coronal Alfvén and magnetosonic waves, and turbulence, but not evaluated here. See works by Wexler et al. (2017) and Jensen, Nolan, et al. (2013) for investigation of the FR fluctuations in these MESSSENGER data, and reports on earlier FR observations by others (Efimov et al., 2015; Chashei et al., 2000; Hollweg et al., 1982, 2010; Andreev et al., 1997).

The radio frequency shift data are shown in Figure 2. The baseband frequency offset (637762.30 Hz) has been removed such that the frequency curve approaches zero in the high-SO limit. We note that the instantaneous frequency shifts are negative since $\frac{d}{dt} N_e$ is negative during egress since number densities are falling with increasing heliocentric distance (see section 4.2), but fractionally less and less so as the LOS egress progresses. The second half of the data show a fairly flat trend but with superimposed low frequency fluctuations. Frequency fluctuations have been studied extensively in coronal radio studies, see Efimov et al. (2017); Yakovlev and Pisanko (2018) for summaries, and Wexler et al. (2019) for a recent MESSENGER-HELIOS composite analysis.

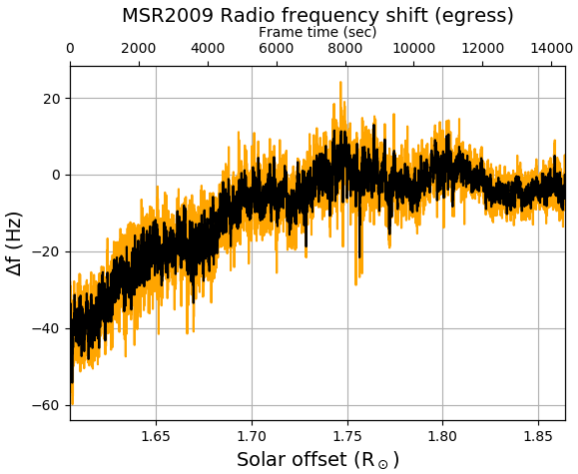

Figure 2. Transcoronal MESSENGER radio frequency observations for 10 Nov 2009. The spacecraft is in egress from solar conjunction; the negative frequency shifts correspond with negative $\frac{d}{dt}N_e$ as the radio signal LOS moves through less dense regions of the corona. The offset-corrected baseband frequency is shown in orange, and the curve smoothed by running 5-point median filter is shown in black.

We can now obtain a rough estimate of the net magnetic field strength component as aligned with the sounding LOS using

$$B_{LOS} = \frac{\Delta\chi}{\xi n_e \Delta S} \tag{4}$$

where Faraday rotation $\Delta\chi$ is 7 radians at SO=1.61, n_e is estimated to be $9 \times 10^{12}\mathrm{m}^{-3}$ using the Allen equation (Allen, 1947) and ξ is given in equation (2). Considering a simple closed magnetic field in the force-free condition, integration path length ΔS to capture the main LOS-aligned field was set equal to the radial distance from the solar surface to the proximate point on the LOS, $0.6\mathrm{R}_\odot = 4.2 \times 10^8\mathrm{m}$. The net magnetic field strength on the LOS in the coronal region of closest solar approach is then ∼5500 nT. It is possible that total B intensties are larger in some regions since the estimate uses only the projection onto LOS. Also, since B_{LOS} is the net sum of local B components, stronger fields of both polarities may be present yet still sum to produce a limited net B strength on the LOS . Using this rough approximation, the Alfvén speed is 40 km/s at the proximate point, but the fairly steep decline in electron density with heliocentric distance should lead to increased Alfvén speeds in other areas along the LOS. We explore these possibilities further after proceeding to a more detailed assessment of the magnetic field and electron densities.

3 CCMC MHD model

The Community Coordinated Modeling Center (CCMC) is a NASA collaborative based at the Goddard Space Flight Center, Greenbelt, MD, offering a variety of solar and heliospheric models (https://ccmc.gsfc.nasa.gov). Coronal models provide 3-D magnetic field solutions based on boundary condition inputs including field strength data from synoptic solar magnetograms. There are a variety of models, each with simplifications and limitations with regards to the underlying coronal physics (MacNeice et al., 2018). The MHD codes are said to produce more realistic cusp topologies beneath streamers compared to the older, Potential Field Source Surface (PFSS) models. Unlike PFSS models, the MHD models do not require a fixed "source surface" beyond which the magnetic fields are radial (Riley et al., 2006). We chose the MHD About a Sphere (MAS) model (Lionello et al., 2009), available

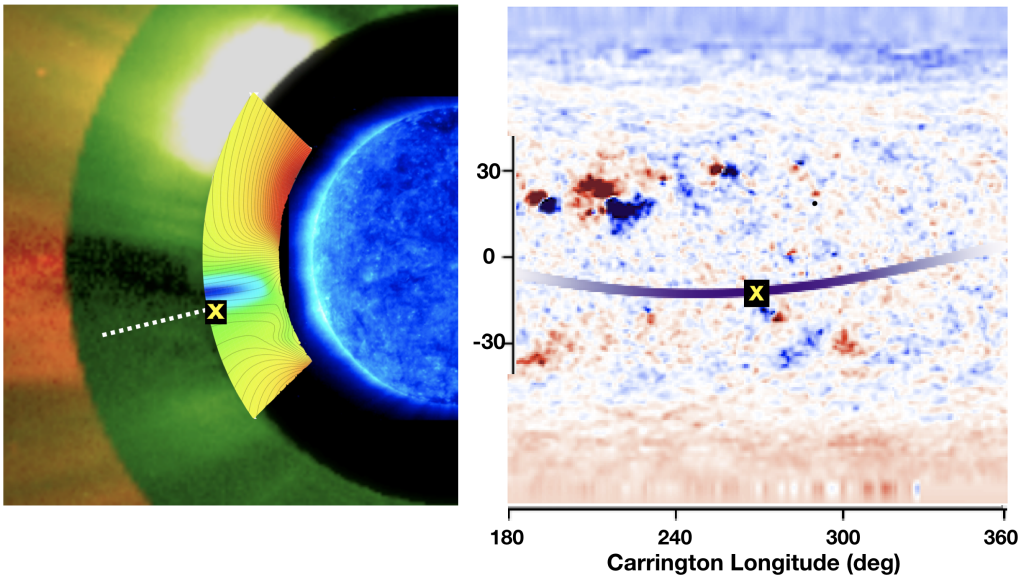

Figure 3. Left: Composite image for 10 November 2009. Streamer patterns are imaged with STEREO B COR1 (green hues) and SOHO LASCO C2 (orange hues) coronagraphs. The COR1 pattern is only approximate for our LOS because STEREO B was obliquely aligned relative to the LOS. The approximate positioning of the LOS proximate points during the MESSENGER observations is shown with the dotted line, and the "X" marks the beginning of the observations at solar offset 1.605$R_\odot$. An overlay strip of MAS model magnetic field output is also shown, with color range in log scale spanning 5.0 (red) to 2.4 (blue) in nT. The solar disk is an EIT 171 image from SOHO. Right: a portion of the GONG synoptic solar surface magnetogram for Carrington rotation 2090. The curved line shows the projection from the spacecraft radio LOS onto the solar surface. The X marks the projection for the point of closest solar approach on the LOS at SO 1.605$R_\odot$.

on the Community Coordinated Modeling Center (CCMC) site. MAS is a so-called "thermodynamic MHD" code, with more detailed handling of energy components in the model compared to a previous polytropic model. We use the MAS 3D coronal model to find the estimated magnetic field vectors along each LOS for the specific Carrington rotation (CR) under study.

Our MAS solution for CR 2090 was produced using CORHEL version 5.0.0 The solution data are archived ("David_Wexler_022117_SH_1") on the CCMC site. The simulations used fixed chromospheric lower-boundary parameters $n_{e0} = 2 \times 10^{18}\mathrm{m}^{-3}$ and $T_0 = 20,000\mathrm{K}$. The code runs in normalized units. Magnetic field output values were converted to Gauss units using the multiplier 2.206 (Lionello et al., 2009). Figure 3, left, shows a strip of the MAS magnetic field output superimposed upon coronagraph images with the egress trajectory marked. Figure 3, right, shows the input solar surface synoptic magnetogram, and the projection of the LOS unto the solar surface, from which each 2-D slice of magnetic field output is aligned to the corresponding path element along the LOS (Figure 3, left). It is noted that the Sun was in moderately low state of activity.

The CCMC MAS computation outputs results into hdf4-formatted data spheres 151 x 100 x 182, in heliographic coordinates (HGC). In contrast, coordinates along the radio sounding LOS coordinates were obtained from the JPL Horizons ephemerides (https://ssd.jpl.nasa.gov/horizons.cgi) in Heliographic Aries Ecliptic (HAE) coordinates. In

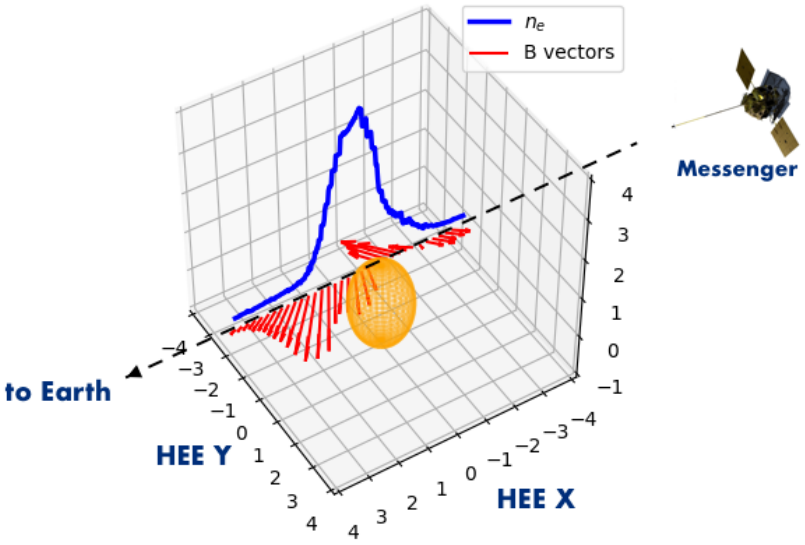

Figure 4. Magnetic field vectors (red) from the CCMC model arranged along the sounding LOS. The field lines are non-radial and asymmetric across the point of closest solar approach. The number density profile (blue) shows near-symmetry with respect to the proximate point. The coordinates are in heliocentric Earth ecliptic (HEE), with positive x being towards Earth.

order to extract the MAS data pertinent to the LOS, the LOS coordinates had to be converted to HGC. The conversions between HAE and HGC were accomplished in accordance with coordinate transformation sequences detailed in Hapgood (1992) and Thompson (2006). The Parker spiral effect is considered negligible at this close offset. The heliographic coordinates for the LOS proximate point at the beginning of the data collection were $r = 1.61 R_\odot$, $\theta = -11.9^o$ and $\phi = 267.7^o$, marked with an X on the mapping in Figure 3. Over the full four hours of observations, coordinate ranges for the proximate point of LOS were 1.61 to 1.86$R_\odot$ for radial distance, -12.0 to -13.1 degrees for heliolatitude and 267.7 to 265.9 degrees for Carrington longitude.

A sample mapping for a specific point on the LOS cutting through the plane at CR longitude 268^o is shown in Figure 3, left. The entire LOS magnetic field mapping, assembling many such planes, captures the magnetic field variations along the LOS (Figure 4). The total field strengths, $|B|$ along the ray paths for three representative SO are mapped along the LOS in Figure 5. Figures 4 and 5 illustrate the non-radial, asymmetric character of the magnetic fields with respect to the point of closest solar approach for the region under study. Field components projected onto the LOS, $B_{||}$, are shown in the results section.

Before generating an FR analysis based on MHD model magnetic field components, we address the electron number densities further and refine the description of n_e using an analytic method that combines the observational frequency shift information with a background power-law model for number density.

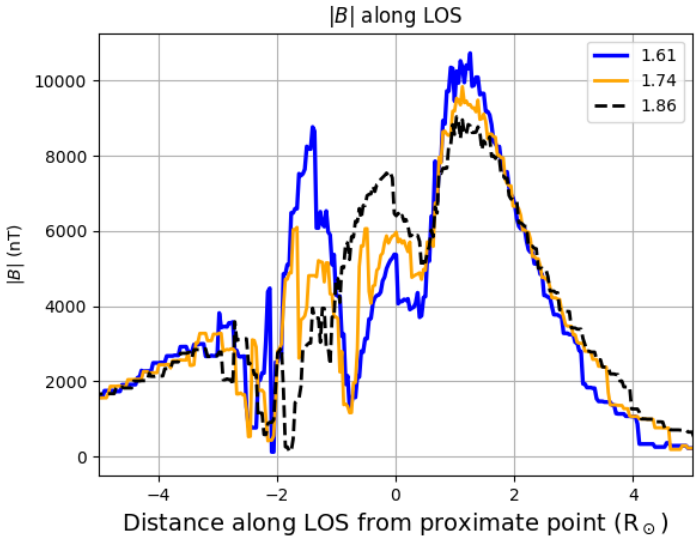

Figure 5. Plots of magnetic field strength along the LOS at three solar offsets, obtained directly from the MAS output data, before final scaling (see §5). The key gives the proximate point offsets in $R_\odot$ units.

4 Electron number density models

4.1 General power-law models

Electron concentrations in the corona are typically modeled as concentric shells, each with number density proportional to the radial offset in a power law format, see e.g. (Kooi et al., 2014; Bird & Edenhofer, 1990). Most models assume radial symmetry, but some account for heliolatitude. The state of solar activity should be specified for a given model. In general, the models are intended to provide average number density estimates. For this study, we sought to revise the number density model for our specific data, by incorporating the frequency shift observational data.

A classic parameter equation for electron concentration in the quiescent equatorial corona, based on white-light eclipse observations, is the Allen-Baumbach equation (Allen, 1947):

$$n_e(r) = 1 \times 10^{14} \left[\frac{2.99}{r^{16}} + \frac{1.55}{r^6} \right] \tag{5}$$

with heliocentric radial distance as ratio r=R/R$_\odot$ and electron concentration in m^{-3}. $R_\odot = 6.96 \times 10^8$m.

Newkirk (1961), also using eclipse data, provided a simpler power law model for the quiet corona electron concentrations:

$$n_e(r) = 14.2 \times 10^{10} 10^{4.32/r} \qquad [m^{-3}] \tag{6}$$

Electron number density models of the corona have also been developed from radio observations. These generally describe the extended corona beyond SO 3R$_\odot$, and are not intended to accurately extrapolate to the inner levels of the corona. Attempts to expand the number density description to incorporate the low-to-middle corona include the composite

formulation given in Wexler et al. (2019)

$$n_e(r) = 1 \times 10^{12} \left[\frac{65}{r^{5.94}} + \frac{0.768}{(r-1)^{2.25}} \right] \qquad [m^{-3}] \tag{7}$$

and the three-term power law model of (Leblanc et al., 1998):

$$n_e(r) = 8.0 \times 10^{13} r^{-6} + 4.1 \times 10^{12} r^{-4} + 3.3 \times 10^{11} r^{-2} \qquad [m^{-3}] \tag{8}$$

In accordance with Leblanc's method to scale the equation to known densities at 1 AU for a given observational time window, we multiplied equation (8) by the factor 5/7.2, where the numerator is average number density at 1 AU from ACE spacecraft data (http://www.srl.caltech.edu/ACE/ASC/). We found that the radial dependence of number density as given from the MAS model was similar to that given by the scaled Leblanc model. However the observations gave indications that electron densities were greatly increased at the lower end of the SO range studied. Using the methods introduced by Efimov and Dolbezhev, and colleagues (Efimov et al., 1990; Dolbezhev et al., 1986), the observed frequency shift Δf was used to revise the Leblanc formula by addition of a fourth power law term. The analysis is presented in the next subsection.

4.2 Radio frequency shift analysis

The observed radio frequency, f_{obs}, is shifted from the original transmitted frequency, f_0 by two major contributions: Doppler shifts due to spacecraft velocity $V_{\rm rel}$ relative to the terrestrial receiving station, and the time-rate of change of electron number densities along the sounding LOS (Vierinen et al., 2014; Jensen et al., 2016):

$$f_{\rm obs} - f_0 = -\frac{V_{\rm rel}}{c} f_0 + \frac{1}{2\pi} r_e \lambda \frac{d}{dt} \int_{\rm LOS} n_e(S,t) dS \tag{9}$$

with radio transmitter wavelength $\lambda = \frac{c}{f_0}$, c the speed of light, n_e the electron number density as a function of position S and time t along the LOS, and $r_e = 2.82 \times 10^{-15}$m is the classical electron radius

$$r_e = \frac{e^2}{4\pi\epsilon_0 m_e c^2}. \tag{10}$$

There is a small effect from gravitational redshift (Bertotti et al., 2003), which changes gradually, less than half a Hz over the observing interval studied, which we ignore here and leave to exploration in subsequent studies. After the Doppler shift is removed, the remaining instantaneous frequency shift Δf_N is attributed to changing electron column density, N_e:

$$\Delta f_N(t) = \frac{1}{2\pi} r_e \lambda \frac{d}{dt} N_e(t). \tag{11}$$

For a given heliocentric distance, r, to the proximate point, the column density for ray path S is

$$N_e(r) = \int_{\rm LOS} n_e(r,S) dS. \tag{12}$$

The orientation of sounding path element dS is assumed to be perpendicular to the direction of r from the heliocenter. The geometric arrangement for analysis of transcoronal radio observations has been described many times, see e.g. (Bird, 1982; Pätzold et al., 1997; Ingleby et al., 2007; Kooi et al., 2014).

Electron column density values cannot be used directly in the calculation of FR since the electron concentrations, like the magnetic field components, are varying along the sounding LOS. Our task is to deduce the radial profile of electron number density from changing column densities. We follow the general approach put forward by Dolbezhev et al. (1986) and Efimov et al. (1990), using their key insight that the parameters in the power law

number density models can be obtained from $\frac{d}{dr}N_e$, which is proportional to the density-change related frequency shift Δf_N. LOS speed on the sky due to projected spacecraft motion, $U_{\rm sc} = \frac{dr}{dt}$, is incorporated into equation (11) to obtain

$$\Delta f_N(r) = \frac{1}{2\pi} r_e \lambda U_{\rm sc} \frac{d}{dr} N_e(r) \tag{13}$$

We now illustrate the analysis using a two-term power law for electron number density. The methods may be generalized to additional terms as warranted. In general, a more limited SO range under study requires fewer terms in the power law expression of number density. However, the study of electron column density entails the integration of number density information over a great distance, from transmitting spacecraft radio to the ground station. Therefore, even in our study involving the limited SO range 1.605-1.864$R_\odot$, for the final implementation we keep all terms.

The dual power law expression of electron number density is

$$n_e(r) = Ar^{-\alpha} + Br^{-\beta} \qquad [m^{-3}] \tag{14}$$

where coefficients A and B are in units m^{-3}.

Following the method of Bird et al. (1994), electron column density, N_e, is found by integration of number density expression applied over the LOS path S (equation 12), generalized to -∞ to ∞. Utilizing Bird's polar transformations $S = R\,tan\,\phi$, $dS = R\,sec^2\,\phi\,d\phi$, the distance L in meters from heliocenter to point S on the LOS becomes $\sqrt{R^2(1+tan^2\,\phi)}$, or $R\,sec\,\phi$. Expressed in units suitable for equation (14), the distance L(ϕ) is $r\,cos^{-1}\,\phi$ and the electron density along the LOS is A$(r\,cos^{-1}\,\phi)^{-\alpha}$+B$(r\,cos^{-1}\,\phi)^{-\beta}$. Completing the column density integral with dS transformed to $rR_\odot\,cos^{-2}\,\phi\,d\phi$ and integrating over limits $-\pi/2$ to $\pi/2$, we find

$$N_e(r) = R_\odot \left[k(\alpha)Ar^{1-\alpha} + k(\beta)Br^{1-\beta}\right] \qquad [m^{-2}] \tag{15}$$

with unitless LOS integration constants

$$k(\alpha) = \sqrt{\pi}\frac{\Gamma(\frac{\alpha-1}{2})}{\Gamma(\frac{\alpha}{2})} \qquad k(\beta) = \sqrt{\pi}\frac{\Gamma(\frac{\beta-1}{2})}{\Gamma(\frac{\beta}{2})}. \tag{16}$$

Note that our convention for solar offset measure, r, leads to reversal of the column density exponent notation compared to that in Bird et al. (1994), e.g. Bird's $\left[\frac{R_\odot}{R}\right]^{\alpha-1}$ vs. our $r^{1-\alpha}$.

Differentiation of equation (15) with respect to radial offset gives

$$\frac{d}{dr}N_e(r) = -R_\odot \left[aAr^{-\alpha} + bBr^{-\beta}\right] \qquad [m^{-2}/R_\odot] \tag{17}$$

or

$$\frac{d}{dR}N_e(r) = -\left[aAr^{-\alpha} + bBr^{-\beta}\right] \qquad [m^{-2}/m] \tag{18}$$

where

$$a = (\alpha-1)k(\alpha) \qquad b = (\beta-1)k(\beta) \tag{19}$$

The frequency shift is therefore related to number density parameters by

$$\Delta f_N(r) = -\frac{1}{2\pi} r_e \lambda U_{\rm sc} \left[aAr^{-\alpha} + bBr^{-\beta}\right] \qquad [Hz] \tag{20}$$

with projected spacecraft speed U_{SC} (in ms^{-1}) defined as positive for egress and negative for ingress, which allows the bracketed quantity in equation (20) to remain positive for purposes of curve-fitting on log-log plots.

Using equation 20 formatted with the scaled Leblanc density model, we found a good fit by least squares for our data over 1.70-1.86$R_\odot$, after removal of the baseband frequency

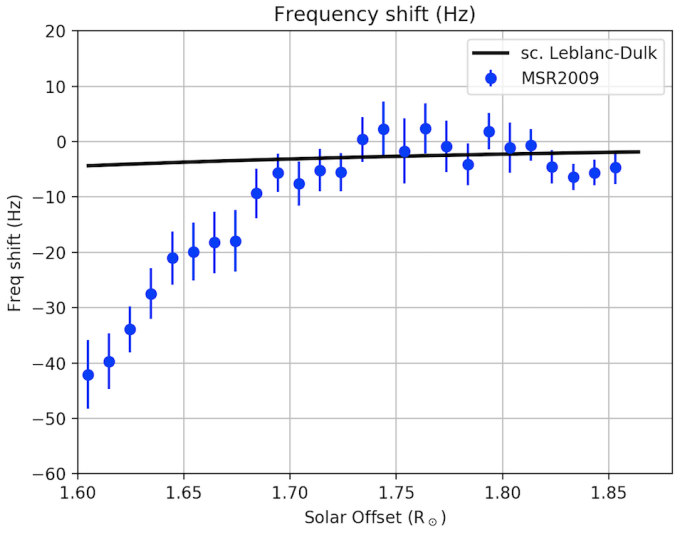

Figure 6. Binned MESSENGER frequency shift data (dots) fitted to the shift predicted using the scaled Leblanc three-component number density model (line). The points between SO 1.70-1.86 were used to fit the model line, using least squares fit. This is the method used to set the baseband frequency offset. The departure of frequency shift below SO 1.70$R_\odot$ is attributed to an increased electron density gradient, to be captured by a fourth power law term added to the Leblanc model.

offset, 637762.30 Hz (Figure 6). Below SO 1.70$R_\odot$, in increased frequency shift suggested higher coronal electron concentrations requiring an additional term to be added to the number density model.

The frequency shift data were converted to the form $\frac{d}{dr}N_e$

$$\frac{d}{dr}N_e = -2\pi\frac{\Delta f_N}{r_e \lambda U_{\rm sc}} \tag{21}$$

which we consider to contain the contributions from the three power law terms of equation (22), and also a fourth term representing the steep increase noted at SO below 1.7$R_\odot$. The fourth term is of the form $Dr^{-\delta}$. Power law exponent δ is found as the log-log slope of the $\frac{d}{dr}N_e$ curve over SO 1.6-1.7$R_\odot$, and coefficient D is found from dividing y-intercept dD by the integration constant d as found in the form of equations (17,19). For our study, the spacecraft radio wavelength is 0.0357m and the sky-projected LOS speed $U_{\rm sc} = 12.7 \times 10^3$ $\rm ms^{-1}$ (egress). We found $D = 1.5 \times 10^{19}$ and $\delta = -29.3$.

The final number density result is

$$n_e(r) = 5.5 \times 10^{13} r^{-6} + 2.8 \times 10^{12} r^{-4} + 2.3 \times 10^{11} r^{-2} + 1.5 \times 10^{19} r^{-29.3} \tag{22}$$

in $\rm m^{-3}$. This formula is intended to represent the radial dependence of n_e only in the limited SO range, coronal location and state of solar activity studied here. The main effect from the fourth power law term in electron density is noted below SO 1.7$R_\odot$. A comparison of the specific number density equation used here in the modeling of FR is compared to those of other n_e models in figure 7.

The steep climb in electron number density below SO=1.7$R_\odot$ is an interesting departure from the general form of typical number density models as shown in Figure 7. The radio signal spectral broadening findings (Figure 1) are consistent with the considerably increased

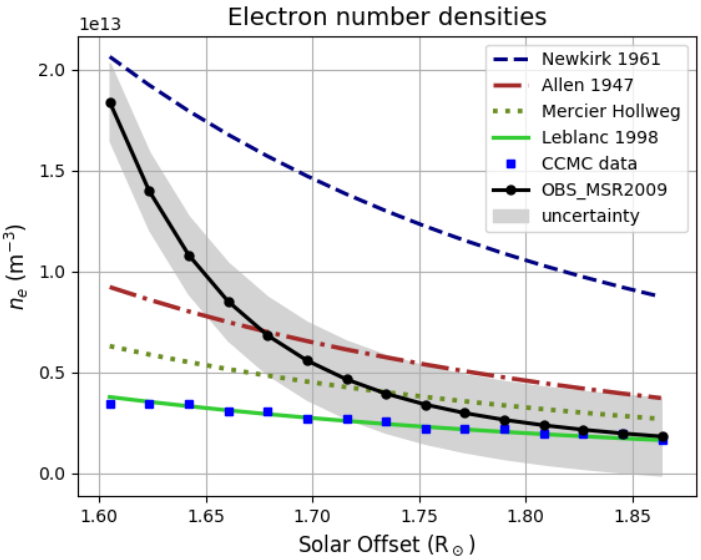

Figure 7. A comparison of electron number density radial profiles. The results of the frequency shift analysis are shown in solid black, revealing a sizable upturn in electron concentration below SO 1.7$R_\odot$. The CCMC MAS model provided n_e values (blue squares) close to those of the native Leblanc three-term equation (solid light green), but did not predict the rise in electron density detected by the frequency shift analysis.

electron density at low SO. The peak value, $n_e = 1.8 \times 10^{13}\mathrm{m}^{-3}$ is realistic and within the range of values for electron density in coronal streamers and quiet Sun regions, see e.g (Guhathakurta & Fisher, 1995; Aschwanden & Acton, 2001; Vocks et al., 2018). The coronal hole plasma exhibits lower densities but relatively steep electron density gradients compared to streamers (Guhathakurta & Fisher, 1995; Hayes et al., 2001). Guhathakurta and Fisher (1995) also showed that streamer boundaries may exhibit similar steep density gradients. Our finding of sharply rising density below SO=1.7$R_\odot$ raises the possibility that the sounding path probed a zone in proximity to a streamer boundary. The available coronagraph imaging does suggest that the sensing LOS traverses the vicinity of a streamer (see Figure 3), although definitive optical evidence of enhanced density specifically at the beginning of the observations is lacking. We view the implied electron density curve as pertaining very specifically to this data set and not suitable for general characterization of the mid-corona. Indeed, the high-order power law exponent could not be applicable down into the lower corona, as the densities would be much too high. We expect additional data sets to reveal more representative density profiles.

5 Results

A hybrid model of FR was produced by combining LOS-projected MAS model magnetic field output with the frequency shift-related electron density profile. As seen in Figure 8, the magnetic field strengths are more variable and widely distributed on the LOS than are the electron densities. Since the FR is calculated by multiplying the local electron number density by the $B_{||}$ at each path LOS element, we find that the number density profile constrains the effective FR region of the LOS for the quiet Sun to about $\pm$ 2$R_\odot$.

In order to match approximately the modeled FR to the observed FR, a small scaling adjustment for MAS model B values was required, and an FR offset was needed for the

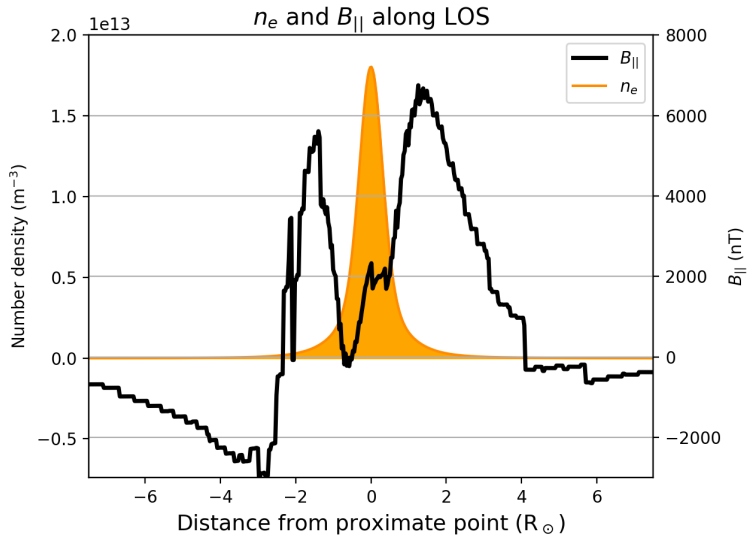

Figure 8. Electron number density profiles (filled area) coplotted with the LOS-aligned magnetic field component, $B_{||}$. The number densities are symmetric across the LOS proximate point (0 on the x-axis), while the FR-effective $B_{||}$ components are asymmetric. The LOS magnetic field convention used here sets a component directed towards Earth on the sounding path as positive. Here the results are presented for SO=1.605R$_\odot$.

observational FR data. We found that the change in polarization position angle, about 7.2 radians, was reproduced by applying a scaling factor of 1.2 to the model magnetic field solution. The suitable FR offset for the observational FR was then found to be 1.8 radians. While the FR offset is arbitrary and was applied primarily for purposes of co-plotting the predicted FR results, it is appropriate that the value be a small value since the FR is expected to diminish with increasing SO, for example seen with FR fluctuations becoming small for X-band radio sounding in the quiet solar corona beyond about 3.5R$_\odot$ (Kobelski et al., 2016). A final offset of 1.8 radians at r=1.86R$_\odot$ is therefore reasonable.

The final results of the FR analysis are shown in Figure 9. The modeled FR curve matches the general form, polarity and magnitude of the observed FR. Uncertainty estimates come from the uncertainty in the frequency shift determinations. An uncertainty of 5Hz for a 42 Hz shift calculates to 12%. Using a fractional error of 0.12 for the observed FR change of 7.24 rads, we expect there is at least 0.9 rad uncertainty in the hybrid model FR predictions. Even with the low-frequency FR oscillations, most of the observations fall within the error bands of the FR model. The main exception was the "transient event" at around SO$\sim$1.66R$_\odot$ during which FR amplitudes were increased. There was no corresponding transient in frequency shift, so on initial consideration it seems likely that the event was predominately a magnetic process. Detailed study of this and other, similar transient FR phenomena will need a separate research effort. Carrington-rotation specific models involve a degree of magnetogram time-averaging over the rotation, and are therefore intended to extract trends and quasi-static features. The method we developed may be useful for the quiescent corona, but less effective for rapidly changing solar environments, for example with CMEs and flares.

Two comments on electron density profiles are in order. First, when the MAS model outputs for electron density were used directly in FR analysis, the observational FR curve was not reproduced. Electron densities from the MAS model produced a flatter FR curve,

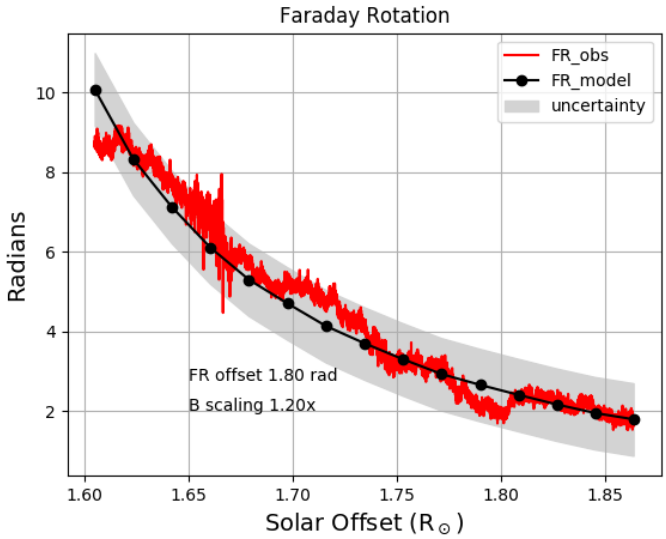

Figure 9. Results of the FR frequency shift-MAS hybrid model (black) plotted over the observational FR data (red). The uncertainly bands (gray) are based on the variance in the frequency shift measurements.

with insufficient FR change, than that observed. A fair fit could be achieved by scaling up the MAS model density curve by 2.5. Second, the observed FR curve is not a shadow curve of the frequency-shift adjusted electron density profile (Figure 7, solid black); the latter has a steeper upturn below SO$\sim 1.7R_{\odot}$. This means the changes in LOS-aligned magnetic field components as a function of solar offset, obtained from the MAS model, also contributed to successful FR modeling.

Since our method links observational FR results to the CCMC MAS model magnetic field components computed from a specific Carrington rotation photospheric magnetogram, the results should be sensitive to exact placement of the LOS in the Carrington heliographic coordinates. We tested this prediction by altering the Carrington longitude coordinate of the CCMC mappings, and comparing the resulting modeled FR to the observed FR curve. For comparison against the correct Carrington longitude for the LOS proximate point, 268^{o}, we ran the model with longitude shifts of -5, -10, -20 and -30 degrees. There is clear progressive departure of the model results from the observed FR as the longitude shift is increased (Figure 10). Although our data set is limited, the appropriate dependence of modeled FR on magnetic map CR longitude provides an encouraging result. Further study using multiple observations through the mid-corona is warranted.

Comparative studies of CCMC coronal-heliospheric models were presented by Jian et al. (2015) and MacNeice et al. (2018). All models underestimated magnetic field strength compared to near-Earth in-situ space observations. The MHD models typically underestimated global open flux at 1 AU by a factor of about two. Interestingly, Jian et al. (2015) found that the coupled MAS corona - ENLIL heliosphere model produced the least underestimation of maximum B strengths, within about 20% of observed values at 1 AU. Our results are consistent with this 20 percent underestimation of B strengths in a new domain, the middle corona, based on transcoronal spacecraft radio FR observations. Since we are using model outputs at relatively low solar offset, close to the photospheric source inputs, we expect a fairly accurate local magnetic field representation near the LOS point of closest solar approach. Whether the B scale factor is consistently about 1.2 in the middle corona with this specific MHD model is an important question for future studies using additional

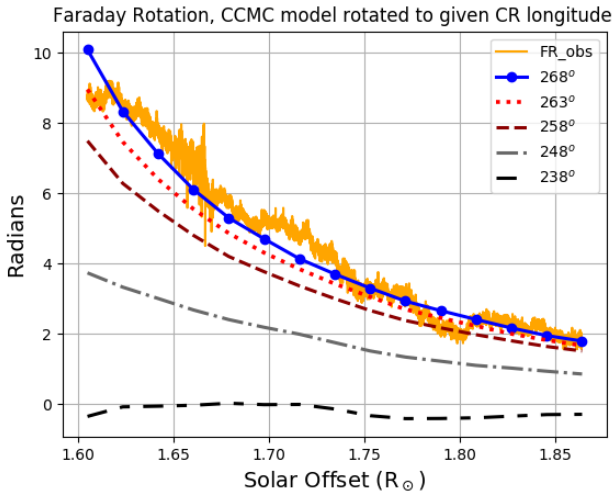

Figure 10. Test of the CCMC magnetic field data. Results with CCMC coronal model rotated into the correct position (CR longitude 268^o) according to the ephemeris localizations of the sounding LOS is shown with the solid blue line (dots were the specific points evaluated). Incremental rotation of the magnetic map Carrington longitude to positions -5, -10, 20 and -30 degrees from the correct longitude resulted in progressively poorer prediction of the observed FR.

data. Also worthwhile will be evaluation of whether the computationally more-efficient PFSS magnetic field methods support FR models consistent with mid-coronal observations.

The range of magnetic field intensities used in the present work fall within the lower end of the range presented by Koutchmy (2004). Through the lower corona region, the field strengths may drop from hundreds of Gauss to about one G. Over SO 1.4-2.5R$_\odot$, which we reference as the middle corona, the few values available in the literature ranged ∼0.08-1 G (8000-100,000 nT). For comparison, our values based on MHD model output along the LOS for SO=1.61R$_\odot$ (Figure 5), and scaling up by x1.2, ranged ∼1000-12000 nT. These values may reflect the LOS positioning through a low field strength sector boundary, and the low global state of solar activity during the observations. On an inverse square potential field basis, 5 nT at 1 AU should be associated with an intensity of 37,000 nT at a 2.5R$_\odot$ source surface, and about 90,000 nT at 1.6R$_\odot$. Values of about 100,0000 nT to 200,000 nT (Mancuso et al., 2019) presented for SO 1.6R$_\odot$ were derived from analysis of CME shock-fronts and solar radio bursts (Gopalswamy et al., 2012; Mancuso et al., 2019, 2003). We do not yet know whether the low-to-middle corona magnetic field intensities are comparable between the impending outburst condition and sustained quiescence. FR measurements are complementary to those of the solar outburst studies; the former do not rely upon sudden dynamic events or other specific activity but assume coronal quasi-stationarity, while the latter probe the inner coronal environment in dynamic conditions. Possibly the idea of "mean coronal magnetic field" will lose generic significance in lower coronal regions where a variety of local activity states and magnetic configurations may coexist.

All FR studies require consideration of the magnetic field structure along the sounding LOS (see Kooi et al. (2014)). In prior FR studies, involving the extended corona over SO $\sim 3-15R_\odot$, the fields were taken to be radial, described by one- or two-term power laws on heliocentric distance, but reversed at a magnetic sector boundary such that non-cancellation of opposing LOS-aligned components resulted in observable FR. These simplifications pose challenges when analyzing specific data sets. For example, Ingleby et al. (2007) required a scale multiplier about 0.475 to bring the modeled FR into line with observations. Also,

Kooi et al. (2014) found that the general power law models tended to over-predict the FR compared to observations over SO 4.6-5.0R$_\odot$. In our study, the magnetic fields varied along the LOS in accordance with the MHD model; we did not assume a radial structure or single sector boundary. Certainly for the sub-streamer coronal regions, the generalized radial models for magnetic field with a single sector line, are unlikely to capture the complex coronal structure or predict the FR evolution during extended observations. Additional data samples will be needed to better characterize the range of conditions and fluctuations encountered in the mid-corona.

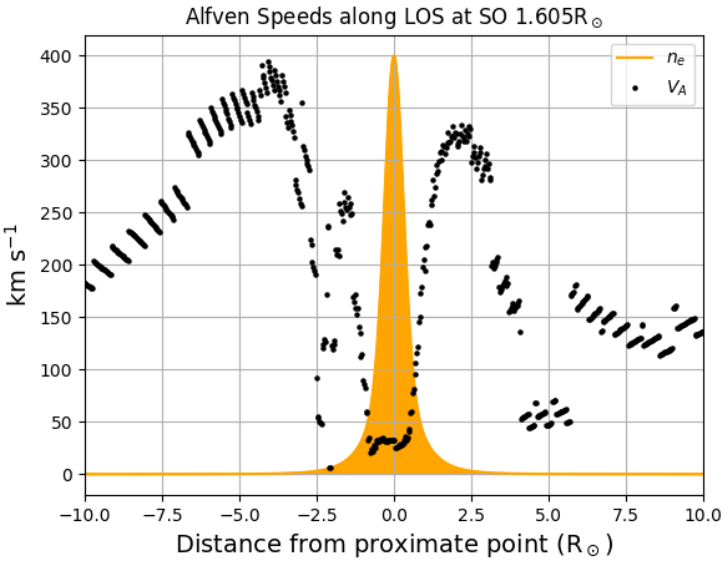

Figure 11. Alfvén wave phase speeds obtained using scaled $|B|$, and n_e profile (unscaled) along the LOS at SO 1.605R$_\odot$.

The complex magnetic spatial variation along the sensing LOS has important implications for MHD wave properties and energetics. We can use the value of n_e and B to estimate the Alfvén wave phase speed,

$$V_A = \frac{B_0}{\sqrt{\mu_0 n_e m_p}} \tag{23}$$

along the the LOS (Figure 11). For this specific coronal region, Alfvén speeds below 50 km/s are found near the point of closest approach but nearly 400 km/s in adjacent regions along the sounding LOS. The radial evolution of Alfvén speeds, like that of the associated magnetic fields (see Figure 5), is variable and at times non-intuitive in the mid-corona. The speeds do not necessarily decrease as a function of SO; rather there may be local maxima and minima. Our range of values for V_A is in the lower half of those summarized by Evans, Opher, Manchester, and Gombosi (2008), which included estimates from the type of MHD model we used (Lionello et al., 2009). Their range of Alfvén speeds through the mid-corona was 100-1500 km s^{-1}, consistent with our belief that a wide range of field strengths will be found in this region. Spatial variation of Alfvén speeds found in sub-streamer, inner-coronal regions as suggested in Figure 11 could promote reflections that induce local wave dissipation, see e.g. (Matthaeus et al., 1999). Thus it is not inconceivable that considerable magnetic wave energy is dissipated into the plasma in the equatorial mid-corona in proximity to zones of initial slow solar wind acceleration.

The Alfvén speeds, together with estimates of magnetic transverse fluctuations, δB, obtained from FR fluctuations studies e.g. (Andreev et al., 1997; Wexler et al., 2017), allow

estimation of Alfvén wave energy flux density. The relatively low magnetic field strengths found here result in low Alfvén wave energy flux locally. Since the Alfvén wave energy scales as $\delta B^2\, V_A$, and δB generally scales with the background field strength, the energy flux density is highly sensitive to magnetic field intensity. Our work suggests that non-uniform MHD wave energy flux should be expected in the mid-corona. The techniques presented here provide a way forward to probe the complex inner coronal regions for study of MHD wave radio signatures and energy transport. We plan to extend our work to these topics in future investigations.

6 Conclusions

In this study we explored a region of the low-latitude middle corona using radio observation techniques, then compared the observed Faraday rotation to that given by a hybrid model based on Community Coordinated Modeling Center MAS ("MHD About a Sphere") magnetic field output and electron density information related to observed frequency shifts. The magnetic field strength values obtained from the CCMC model produced results consistent with the observed FR when scaled up by 20%. Our example demonstrates the potential value of the model as applied in complex coronal magnetic structures, provided the field may be considered quasi-stable in the given Carrington rotation. We expect the model would be less useful in active solar conditions with relatively rapidly changing magnetic field conditions and eruptive events. Nevertheless, if confirmed with additional data, the hybrid approach combining frequency-shift observations with MHD model fields will break new ground in enabling detailed analysis of deep coronal regions without the assumptions of simplified field geometry or dependence on solar outburst events.

Electron number density curves obtained directly from the MAS model were too low to achieve the amount and form of the observed FR. However, when the Leblanc electron density model was adjusted using radio frequency shift data, the resulting four-term power law for electron density (equation 22) led to good concordance with FR observations. Although generally consistent with previous parameter model approximations of average n_e, the frequency-shift method provided additional detail specific to this particular data segment. A steep rise in electron concentrations below SO $1.7 R_\odot$ was found. We speculate that this density pattern may be related to steep gradients near a streamer boundary (Guhathakurta & Fisher, 1995), but also note the order-of-magnitude density changes recently reported in within white-light streamer structures (DeForest et al., 2018). Further studies using the frequency-shift analysis in the middle corona should contribute new insights about variations in plasma density structure.

Incorporation of MHD models into observation-based analysis should advance our understanding of coronal energy transport and acceleration of the solar-wind. The coronal magnetic field is a key pillar of coronal organization and dynamics. Our findings indicate that the low-latitude middle corona includes non-radial and asymmetric magnetic fields. From the variability in field intensity along the LOS we infer that a range of Alfvén wave speeds and MHD wave energies will be found in the mid-corona, with non-uniform distribution. A broad radio observing campaign will be needed to accumulate data from mulitple sites and solar activity levels to confirm these impressions. As additional analyses are conducted, a more complete picture of the challenging mid-coronal magnetic landscape will emerge, allowing MHD wave heating and other mechanisms (Cranmer et al., 2015; Woolsey & Cranmer, 2015) to be more thoroughly evaluated.

Acknowledgments

The authors thank Carl Heiles, Amanda Kepley and Divya Oberoi for helpful information and discussions. We also thank Ariel Wexler for computing and coding advice. Special appreciation to Peter Macniece and the Community Coordinated Modeling Center team for providing the MAS output files and technical guidance. We appreciate the comments and improvements offered by the reviewers. The observational data for this study are available on the CEDAR Madrigal database (Green Bank Telescope, 2009):
http://cedar.openmadrigal.org/showExperiment/?experiment_list=experiments/2009/gbt/10nov09&file_list=gbt20091110.001.h5

D.W. thanks Stephen Marsden at the University of Southern Queensland for administrative academic supervision and the MIT Haystack Observatory for providing local research office support and mentoring.

References

Abbo, L., Ofman, L., Antiochos, S. K., Hansteen, V. H., Harra, L., Ko, Y.-K., ... Wang, Y.-M. (2016, November). Slow Solar Wind: Observations and Modeling. *Space Science Rev.*, *201*, 55-108. doi: 10.1007/s11214-016-0264-1

Allen, C. W. (1947). Interpretation of Electron Densities from Corona Brightness. *Mon Notices Royal Astron Soc*, *107*, 426. doi: 10.1093/mnras/107.5-6.426

Andreev, V. E., Efimov, A. I., Samoznaev, L. N., Chashei, I. V., & Bird, M. K. (1997, January). Properties of coronal Alfven waves from polarized radio occultation experiments. *Advances in Space Research*, *20*, 65. doi: 10.1016/S0273-1177(97)00482-1

Arregui, I. (2015, April). Wave heating of the solar atmosphere. *Philosophical Transactions of the Royal Society of London Series A*, *373*, 20140261-20140261. doi: 10.1098/rsta.2014.0261

Aschwanden, M. J., & Acton, L. W. (2001, March). Temperature Tomography of the Soft X-Ray Corona: Measurements of Electron Densities, Tempuratures, and Differential Emission Measure Distributions above the Limb. *Astrophys J.*, *550*, 475-492. doi: 10.1086/319711

Badalyan, O. G. (1996). Temperature and Density in the Middle Corona Through the Activity Cycle Determined from White Light Observations. *Astronomical and Astrophysical Transactions*, *9*, 205-223. doi: 10.1080/10556799608208224

Bastian, T. S. (2001, June). Radio Wave Propagation in the Corona and the Interplanetary Medium. *Astrophys Space Sci*, *277*, 107-116. doi: 10.1023/A:1012232111843

Bertotti, B., Iess, L., & Tortora, P. (2003, September). A test of general relativity using radio links with the Cassini spacecraft. *Nature*, *425*, 374-376. doi: 10.1038/nature01997

Bird, M. K. (1982, March). Coronal investigations with occulted spacecraft signals. *Space Sci Rev*, *33*, 99-126. doi: 10.1007/BF00213250

Bird, M. K. (2007, December). Coronal Faraday rotation of occulted radio signals. *Astronomical and Astrophysical Transactions*, *26*, 441-453. doi: 10.1080/10556790701595236

Bird, M. K., & Edenhofer, P. (1990). Remote Sensing Observations of the Solar Corona. In R. Schwenn & E. Marsch (Eds.), *Physics of the inner heliosphere I* (p. 13).

Bird, M. K., Volland, H., Paetzold, M., Edenhofer, P., Asmar, S. W., & Brenkle, J. P. (1994, May). The Coronal Electron Density Distribution Determined from Dual-Frequency Ranging Measurements during the 1991 Solar Conjunction of the ULYSSES Spacecraft. *Astrophys J.*, *426*, 373. doi: 10.1086/174073

Brooks, D. H., Ugarte-Urra, I., & Warren, H. P. (2015, January). Full-Sun observations for identifying the source of the slow solar wind. *Nature Communications*, *6*, 5947. doi: 10.1038/ncomms6947

Chashei, I. V., Efimov, A. I., Samoznaev, L. N., Bird, M. K., & Pätzold, M. (2000). The Spectrum of Magnetic Field Irregularities in the Solar Corona and in Interplanetary

Space. *Advances in Space Research*, *25*, 1973-1978. doi: 10.1016/S0273-1177(99)00614-6

Cranmer, S. R., Asgari-Targhi, M., Miralles, M. P., Raymond, J. C., Strachan, L., Tian, H., & Woolsey, L. N. (2015, April). The role of turbulence in coronal heating and solar wind expansion. *Philosophical Transactions of the Royal Society of London Series A*, *373*, 20140148-20140148. doi: 10.1098/rsta.2014.0148

DeForest, C. E., Howard, R. A., Velli, M., Viall, N., & Vourlidas, A. (2018, July). The Highly Structured Outer Solar Corona. *Astrophys J.*, *862*, 18. doi: 10.3847/1538-4357/aac8e3

Dolbezhev, G. G., Efimov, A. I., Tikhonov, V. F., & Yakovlev, O. I. (1986, February). Frequency variations during radio-wave propagation through the circumsolar plasma. *Radiotekhnika i Elektronika (Soviet Journal of Communication and Electronics*, *31*, 354-360.

Efimov, A. I., Lukanina, L. A., Chashei, I. V., Bird, M. K., Pätzold, M., & Wexler, D. (2018, November). Velocity of the Inner Solar Wind from Coronal Sounding Experiments with Spacecraft. *Cosmic Research*, *56*, 405-410. doi: 10.1134/S0010952518060023

Efimov, A. I., Lukanina, L. A., Rogashkova, A. I., Samoznaev, L. N., Chashei, I. V., Bird, M. K., & Pätzold, M. (2015, April). Faraday-rotation fluctuations from radio-sounding measurements of the circumsolar plasma using polarized signals from the HELIOS-1 and HELIOS-2 space probes. *Astronomy Reports*, *59*, 313-326. doi: 10.1134/S1063772915040022

Efimov, A. I., Lukanina, L. A., Samoznaev, L. N., Chashei, I. V., Bird, M. K., & Pätzold, M. (2017, March). Frequency fluctuations in the solar corona investigated with radio sounding experiments on the spacecraft ROSETTA and MARS EXPRESS in 2010/2011. *Advances in Space Research*, *59*, 1652-1662. doi: 10.1016/j.asr.2017.01.001

Efimov, A. I., Yakovlev, O. I., Vyshlov, A. S., Nabatov, A. S., & Laptev, N. V. (1990, September). Frequency changes and refraction during radio wave propagation through solar wind plasma. *Radiofizika*, *33*, 1007-1012. doi: 10.1007/BF01050512

Evans, R. M., Opher, M., Manchester, W. B., IV, & Gombosi, T. I. (2008, November). Alfvén Profile in the Lower Corona: Implications for Shock Formation. *Astrophys J.*, *687*, 1355-1362. doi: 10.1086/592016

Gopalswamy, N., Nitta, N., Akiyama, S., Mäkelä, P., & Yashiro, S. (2012, January). Coronal Magnetic Field Measurement from EUV Images Made by the Solar Dynamics Observatory. *Astrophys. J.*, *744*, 72. doi: 10.1088/0004-637X/744/1/72

Guhathakurta, M., & Fisher, R. R. (1995). Coronal streamers and fine scale structures of the low latitude corona as detected with Spartan 201-01 White Light Coronagraph. *Geophys Res Ltr*, *22*, 1841-1844. doi: 10.1029/95GL01603

Hapgood, M. A. (1992). Space physics coordinate transformations - a user guide. *Planetary Space Sci*, *40*, 711–717. doi: 10.1016/0032-0633(92)90012-D

Hayes, A. P., Vourlidas, A., & Howard, R. A. (2001, February). Deriving the Electron Density of the Solar Corona from the Inversion of Total Brightness Measurements. *Astrophys J.*, *548*, 1081-1086. doi: 10.1086/319029

Hollweg, J. V., Bird, M. K., Volland, H., Edenhofer, P., Stelzried, C. T., & Seidel, B. L. (1982, January). Possible evidence for coronal Alfven waves. *J. Geophys Res*, *87*, 1-8. doi: 10.1029/JA087iA01p00001

Hollweg, J. V., Cranmer, S. R., & Chandran, B. D. G. (2010, October). Coronal Faraday Rotation Fluctuations and a Wave/Turbulence-driven Model of the Solar Wind. *Astrophys J.*, *722*, 1495-1503. doi: 10.1088/0004-637X/722/2/1495

Ingleby, L. D., Spangler, S. R., & Whiting, C. A. (2007, October). Probing the Large-Scale Plasma Structure of the Solar Corona with Faraday Rotation Measurements. *Astrophys J.*, *668*, 520-532. doi: 10.1086/521140

Jensen, E. A., Bird, M. K., Asmar, S. W., Iess, L., Anderson, J. D., & Russell, C. T. (2005). The Cassini solar Faraday rotation experiment. *Advances in Space Research*, *36*, 1587-1594. doi: 10.1016/j.asr.2005.09.039

Jensen, E. A., Bisi, M. M., Breen, A. R., Heiles, C., Minter, T., & Vilas, F. (2013, July). Measurements of Faraday Rotation Through the Solar Corona During the 2009 Solar Minimum with the MESSENGER Spacecraft. *Solar Phys*, *285*, 83-95. doi: 10.1007/s11207-012-0213-4

Jensen, E. A., Frazin, R., Heiles, C., Lamy, P., Llebaria, A., Anderson, J. D., ... Fallows, R. A. (2016, February). The Comparison of Total Electron Content Between Radio and Thompson Scattering. *Solar Phys.*, *291*, 465-485. doi: 10.1007/s11207-015-0834-5

Jensen, E. A., Nolan, M., Bisi, M. M., Chashei, I., & Vilas, F. (2013, July). MESSENGER Observations of Magnetohydrodynamic Waves in the Solar Corona from Faraday Rotation. *solar Phys*, *285*, 71-82. doi: 10.1007/s11207-012-0162-y

Jian, L. K., MacNeice, P. J., Taktakishvili, A., Odstrcil, D., Jackson, B., Yu, H.-S., ... Evans, R. M. (2015). Validation for solar wind prediction at Earth: Comparison of coronal and heliospheric models installed at the CCMC. *Space Weather*, *13*, 316-338. doi: 10.1002/2015SW001174

Kobelski, A., Jensen, E., Wexler, D., Heiles, C., Kepley, A., Kuiper, T., & Bisi, M. (2016). Measuring the Solar Magnetic Field with STEREO A Radio Transmissions: Faraday Rotation Observations using the 100m Green Bank Telescope. In I. Dorotovic, C. E. Fischer, & M. Temmer (Eds.), *Coimbra solar physics meeting: Ground-based solar observations in the space instrumentation era* (Vol. 504, p. 99).

Kooi, J. E. (2016). *Very large array faraday rotation studies of the coronal plasma* (Unpublished doctoral dissertation). The University of Iowa.

Kooi, J. E., Fischer, P. D., Buffo, J. J., & Spangler, S. R. (2014, March). Measurements of Coronal Faraday Rotation at 4.6 R . *Astrophys J.*, *784*, 68. doi: 10.1088/0004-637X/784/1/68

Koutchmy, S. (2004). Structure and Dynamics of the Solar Corona. In A. V. Stepanov, E. E. Benevolenskaya, & A. G. Kosovichev (Eds.), *Multi-wavelength investigations of solar activity* (Vol. 223, p. 509-516). doi: 10.1017/S1743921304006702

Le Chat, G., Kasper, J. C., Cohen, O., & Spangler, S. R. (2014, July). Diagnostics of the Solar Corona from Comparison between Faraday Rotation Measurements and Magnetohydrodynamic Simulations. *Astrophys J.*, *789*, 163. doi: 10.1088/0004-637X/789/2/163

Leblanc, Y., Dulk, G. A., & Bougeret, J.-L. (1998, November). Tracing the Electron Density from the Corona to 1au. *Solar Phys*, *183*, 165-180. doi: 10.1023/A:1005049730506

Lionello, R., Linker, J. A., & Mikić, Z. (2009, January). Multispectral Emission of the Sun During the First Whole Sun Month: Magnetohydrodynamic Simulations. *Astrophys J.*, *690*, 902-912. doi: 10.1088/0004-637X/690/1/902

MacNeice, P., Jian, L. K., Antiochos, S. K., Arge, C. N., Bussy-Virat, C. D., DeRosa, M. L., ... Sokolov, I. (2018, November). Assessing the Quality of Models of the Ambient Solar Wind. *Space Weather*, *16*, 1644-1667. doi: 10.1029/2018SW002040

Mancuso, S., Frassati, F., Bemporad, A., & Barghini, D. (2019, April). Three-dimensional reconstruction of CME-driven shock-streamer interaction from radio and EUV observations: a different take on the diagnostics of coronal magnetic fields. , *624*, L2. doi: 10.1051/0004-6361/201935157

Mancuso, S., & Garzelli, M. V. (2013a, December). Coronal magnetic field strength from Type II radio emission: complementarity with Faraday rotation measurements. *Astron Astrophys*, *560*, L1. doi: 10.1051/0004-6361/201322645

Mancuso, S., & Garzelli, M. V. (2013b, May). Radial profile of the inner heliospheric magnetic field as deduced from Faraday rotation observations. *Astron Astrophys*, *553*, A100. doi: 10.1051/0004-6361/201220319

Mancuso, S., & Garzelli, M. V. (2013c). Using Faraday Rotation to Infer the Inner Heliospheric Radial Magnetic Field. *Central European Astrophysical Bulletin*, *37*, 631-636.

Mancuso, S., Raymond, J. C., Kohl, J., Ko, Y.-K., Uzzo, M., & Wu, R. (2003, March). Plasma properties above coronal active regions inferred from SOHO/UVCS and radio spectrograph observations. *Astron Astrophys*, *400*, 347-353. doi: 10.1051/0004-6361:20021844

Matthaeus, W. H., Zank, G. P., Oughton, S., Mullan, D. J., & Dmitruk, P. (1999, September). Coronal Heating by Magnetohydrodynamic Turbulence Driven by Reflected Low-Frequency Waves. *Astrrophys J Ltr*, *523*, L93-L96. doi: 10.1086/312259

Newkirk, G., Jr. (1961, May). The Solar Corona in Active Regions and the Thermal Origin of the Slowly Varying Component of Solar Radio Radiation. *Astrophys J.*, *133*, 983. doi: 10.1086/147104

Ofman, L., & Wang, T. J. (2008, May). Hinode observations of transverse waves with flows in coronal loops. *Astron Astrophys.*, *482*, L9-L12. doi: 10.1051/0004-6361:20079340

Pätzold, M., Bird, M. K., Volland, H., Levy, G. S., Seidel, B. L., & Stelzried, C. T. (1987, September). The mean coronal magnetic field determined from HELIOS Faraday rotation measurements. *Solar Phys*, *109*, 91-105. doi: 10.1007/BF00167401

Pätzold, M., Tsurutani, B. T., & Bird, M. K. (1997, October). An estimate of large-scale solar wind density and velocity profiles in a coronal hole and the coronal streamer belt. *J. Geophys Res*, *102*, 24151-24160. doi: 10.1029/97JA01868

Riley, P., Linker, J. A., Mikić, Z., Lionello, R., Ledvina, S. A., & Luhmann, J. G. (2006). A comparison between global solar magnetohydrodynamic and potential field source surface model results. *Astrophys J*, *653*, 1510–1516. doi: 10.1086/508565

Sheeley, N. R., Wang, Y.-M., Hawley, S. H., Brueckner, G. E., Dere, K. P., Howard, R. A., ... Biesecker, D. A. (1997, July). Measurements of Flow Speeds in the Corona Between 2 and 30 R. *Astrophys J.*, *484*, 472-478. doi: 10.1086/304338

Thompson, W. T. (2006). Coordinate systems for solar image data. *Astron Astrophys*, *449*, 791–803. doi: 10.1051/0004-6361:20054262

Verwichte, E., Aschwanden, M. J., Van Doorsselaere, T., Foullon, C., & Nakariakov, V. M. (2009, June). Seismology of a Large Solar Coronal Loop from EUVI/STEREO Observations of its Transverse Oscillation. *Astrophys J.*, *698*, 397-404. doi: 10.1088/0004-637X/698/1/397

Vierinen, J., Norberg, J., Lehtinen, M. S., Amm, O., Roininen, L., Väänänen, A., ... McKay-Bukowski, D. (2014, December). Beacon satellite receiver for ionospheric tomography. *Radio Science*, *49*, 1141-1152. doi: 10.1002/2014RS005434

Vocks, C., Mann, G., Breitling, F., Bisi, M. M., Dąbrowski, B., Fallows, R., ... Rucker, H. (2018, June). LOFAR observations of the quiet solar corona. *Astron Astrophys.*, *614*, A54. doi: 10.1051/0004-6361/201630067

Wexler, D. B., Hollweg, J. V., Efimov, A. I., Lukanina, L. A., Coster, A. J., Vierinen, J., & Jensen, E. A. (2019). Spacecraft Radio Frequency Fluctuations in the Solar Corona: A MESSENGERHELIOS Composite Study. *Astrophys J.*.

Wexler, D. B., Jensen, E. A., Hollweg, J. V., Heiles, C., Efimov, A. I., Vierinen, J., & Coster, A. J. (2017, February). Faraday rotation fluctuations of MESSENGER radio signals through the equatorial lower corona near solar minimum. *Space Weather*, *15*, 310-324. doi: 10.1002/2016SW001558

Woch, J., Axford, W. I., Mall, U., Wilken, B., Livi, S., Geiss, J., ... Forsyth, R. J. (1997, November). SWICS/Ulysses observations: The three-dimensional structure of the heliosphere in the declining/minimum phase of the solar cycle. *Geophys Res Letters*, *24*, 2885-2888. doi: 10.1029/97GL01605

Woo, R., Yang, F.-C., & Ishimaru, A. (1976, December). Structure of density fluctuations near the Sun deduced from Pioneer-6 spectral broadening measurements. *Astrophys J.*, *210*, 593-602. doi: 10.1086/154864

Woolsey, L. N., & Cranmer, S. R. (2015, Oct). Time-dependent Turbulent Heating of Open Flux Tubes in the Chromosphere, Corona, and Solar Wind. *Astrophys. J.*, *811*(2), 136. doi: 10.1088/0004-637X/811/2/136

Yakovlev, O. I., & Pisanko, Y. V. (2018, January). Radio sounding of the solar wind acceleration region with spacecraft signals. *Advances in Space Research*, *61*, 552-566. doi: 10.1016/j.asr.2017.10.052

Figure 1.

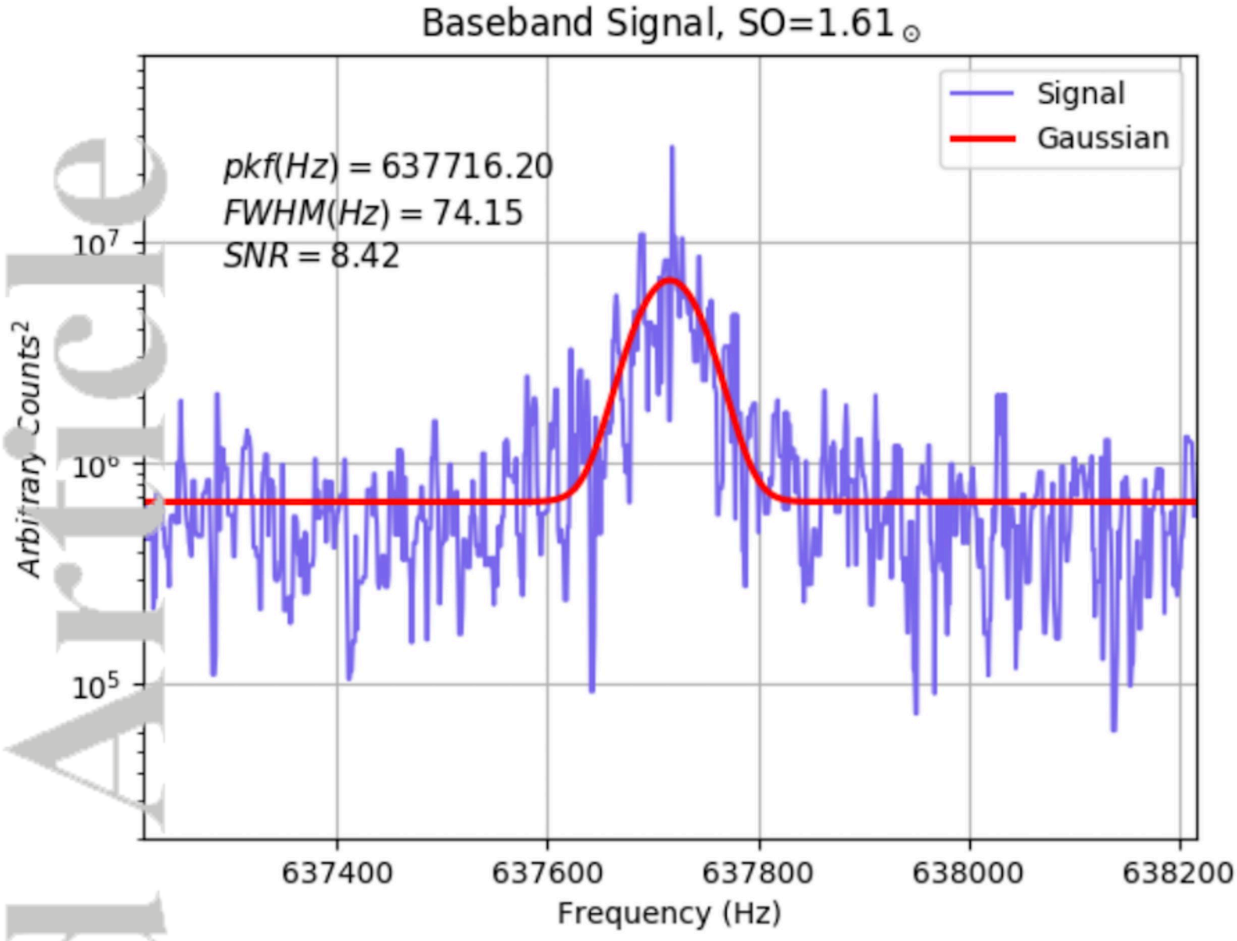

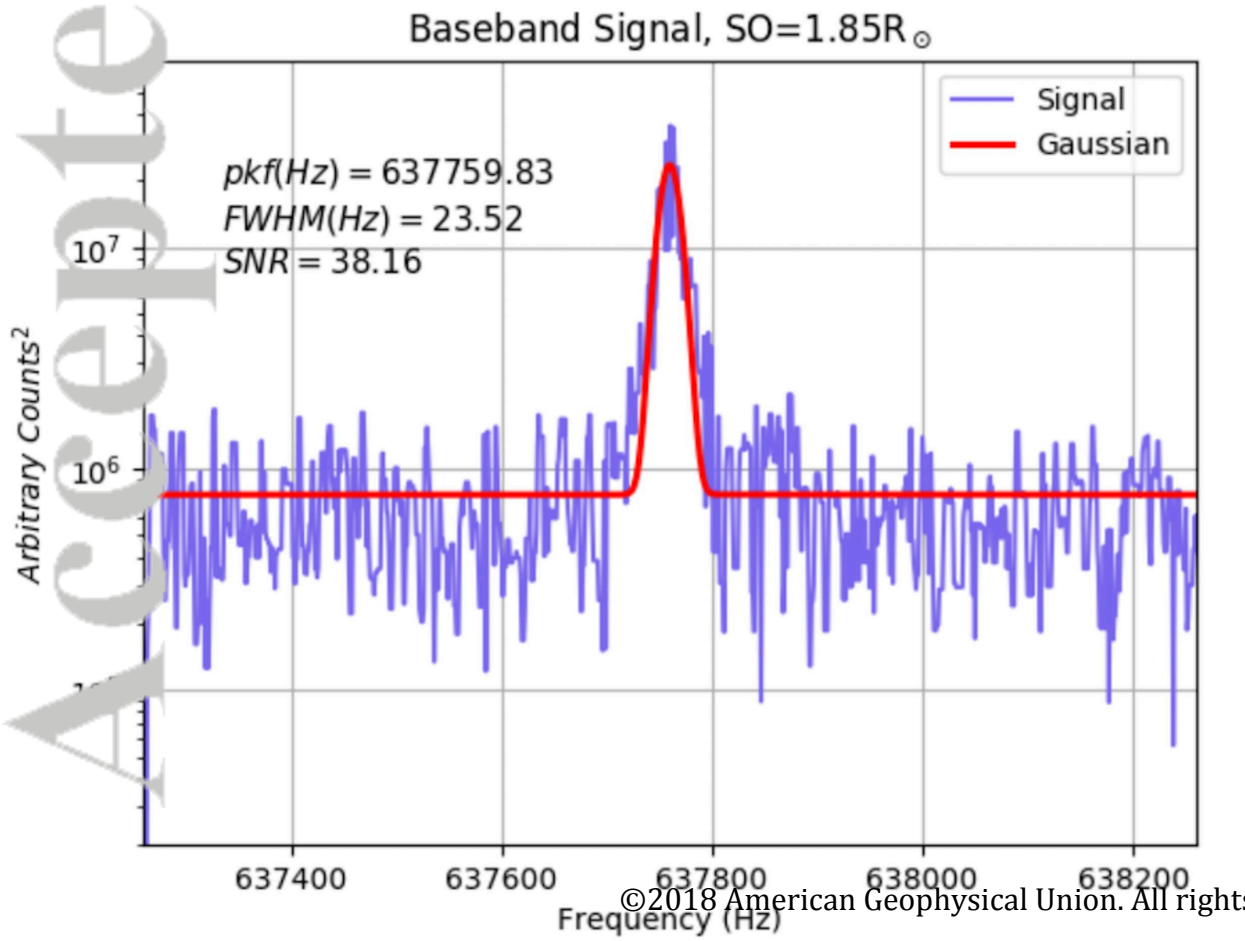

Figure 2.

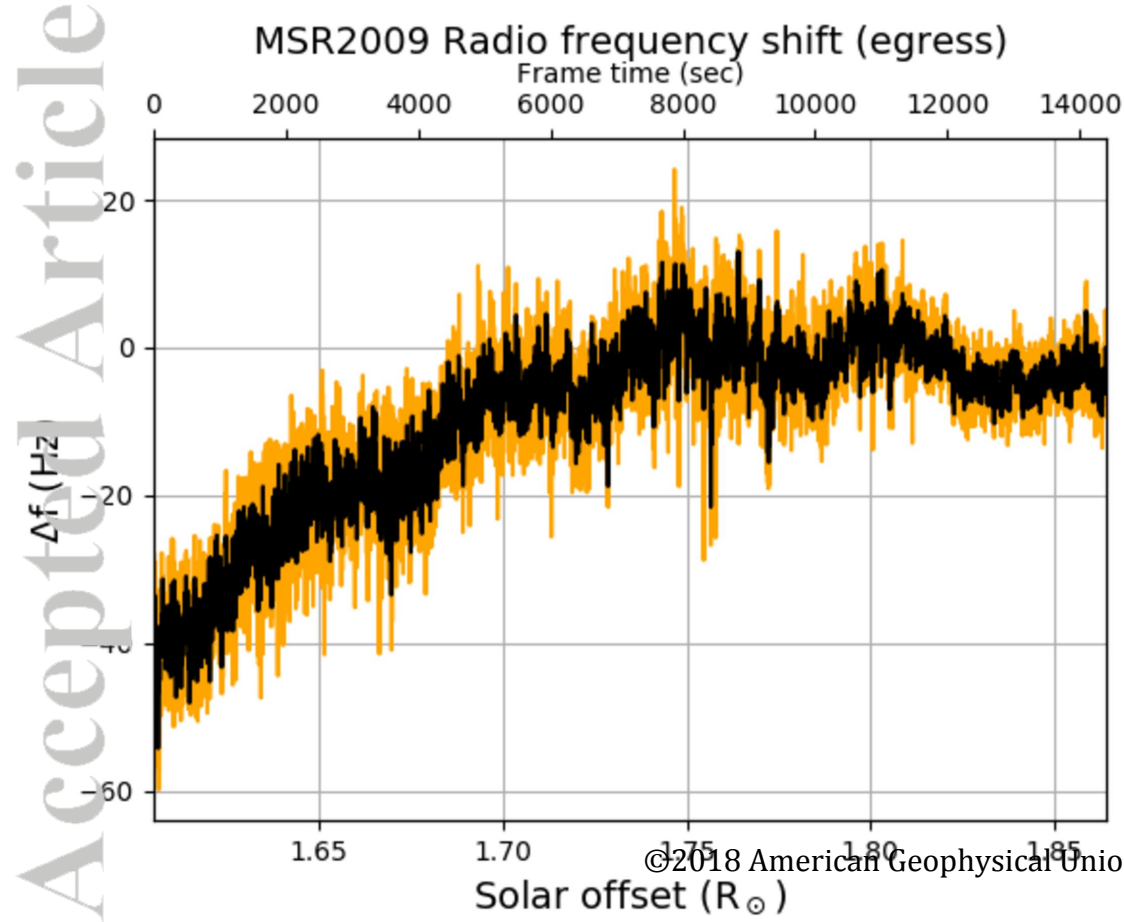

Figure 3.

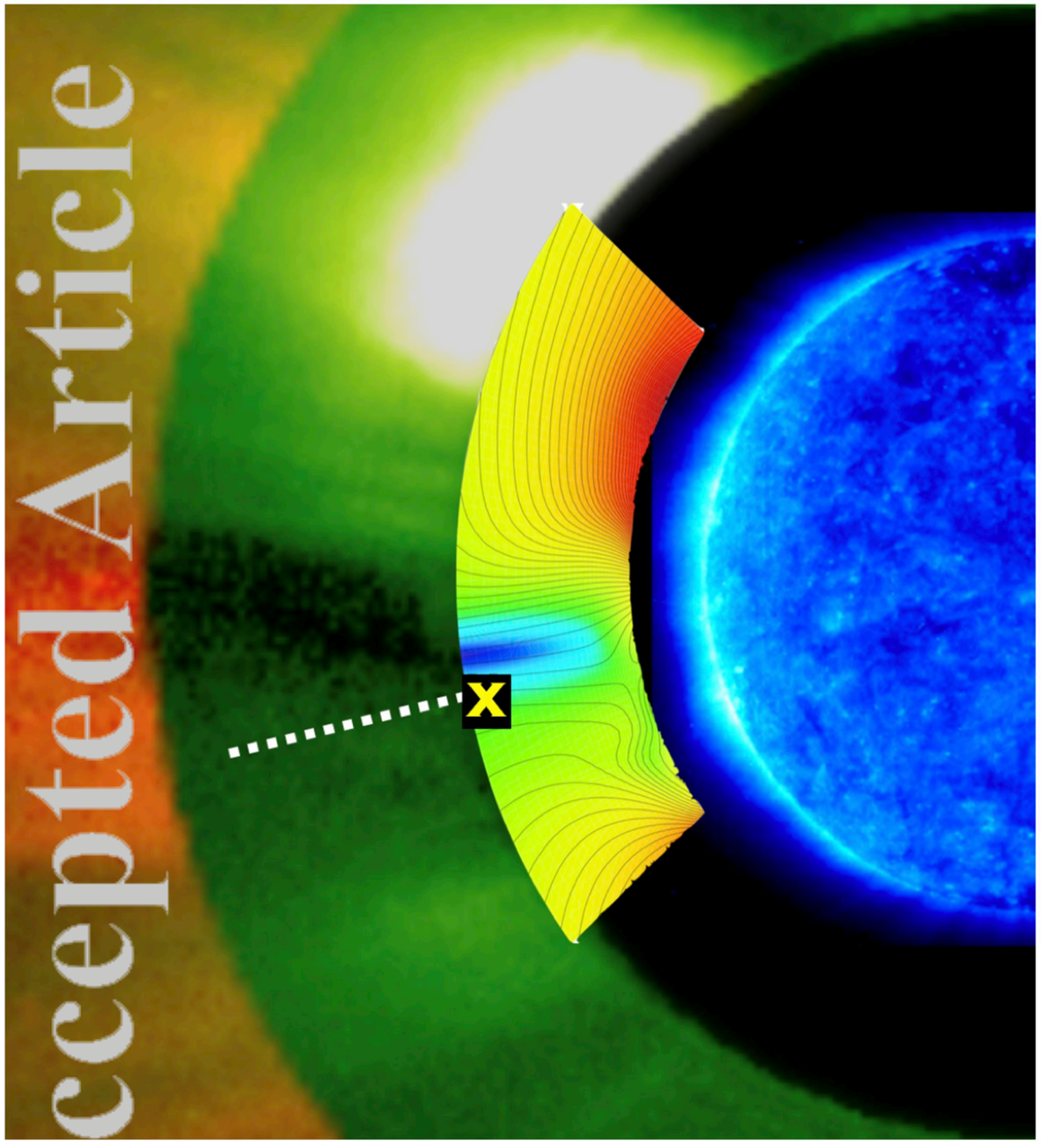

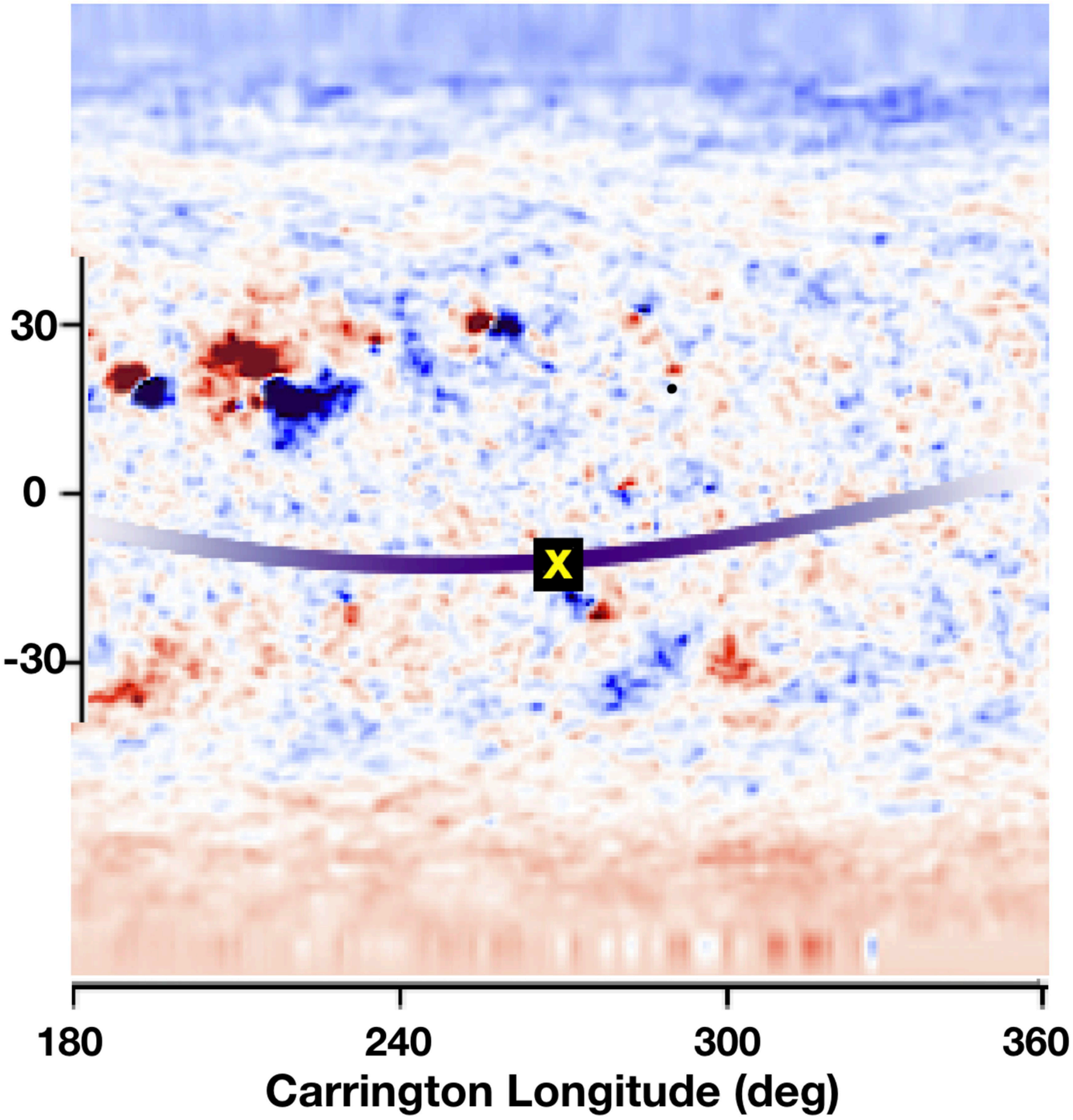

Figure 4.

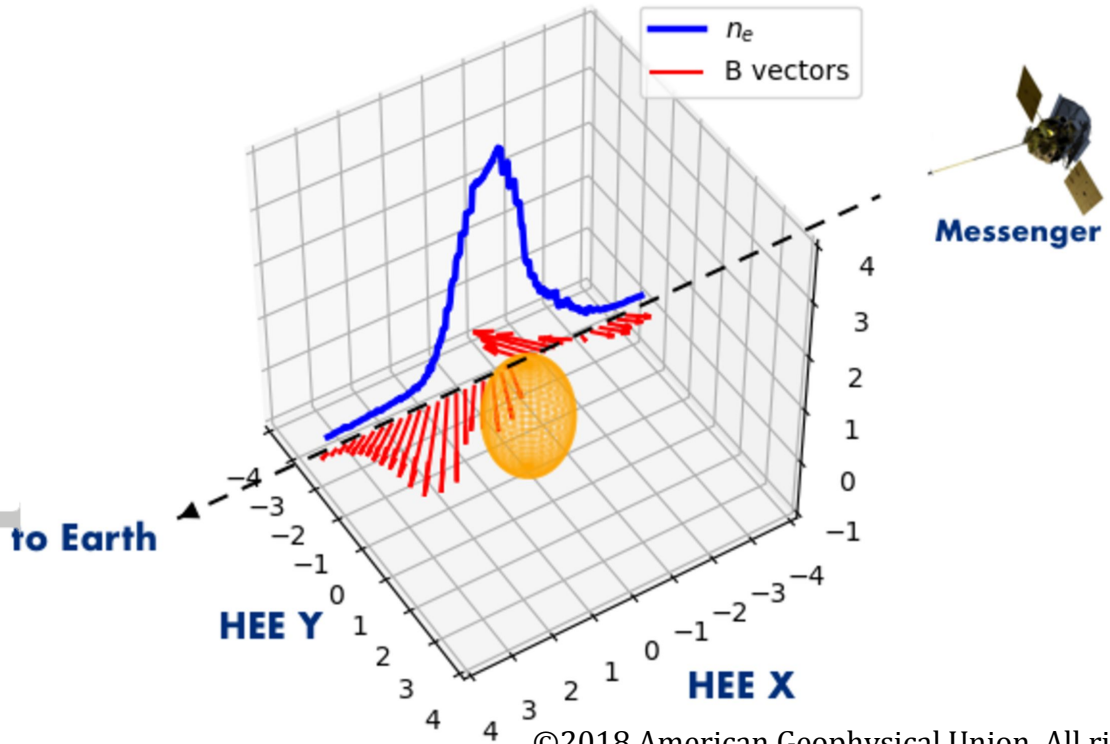

FIGURE 5.

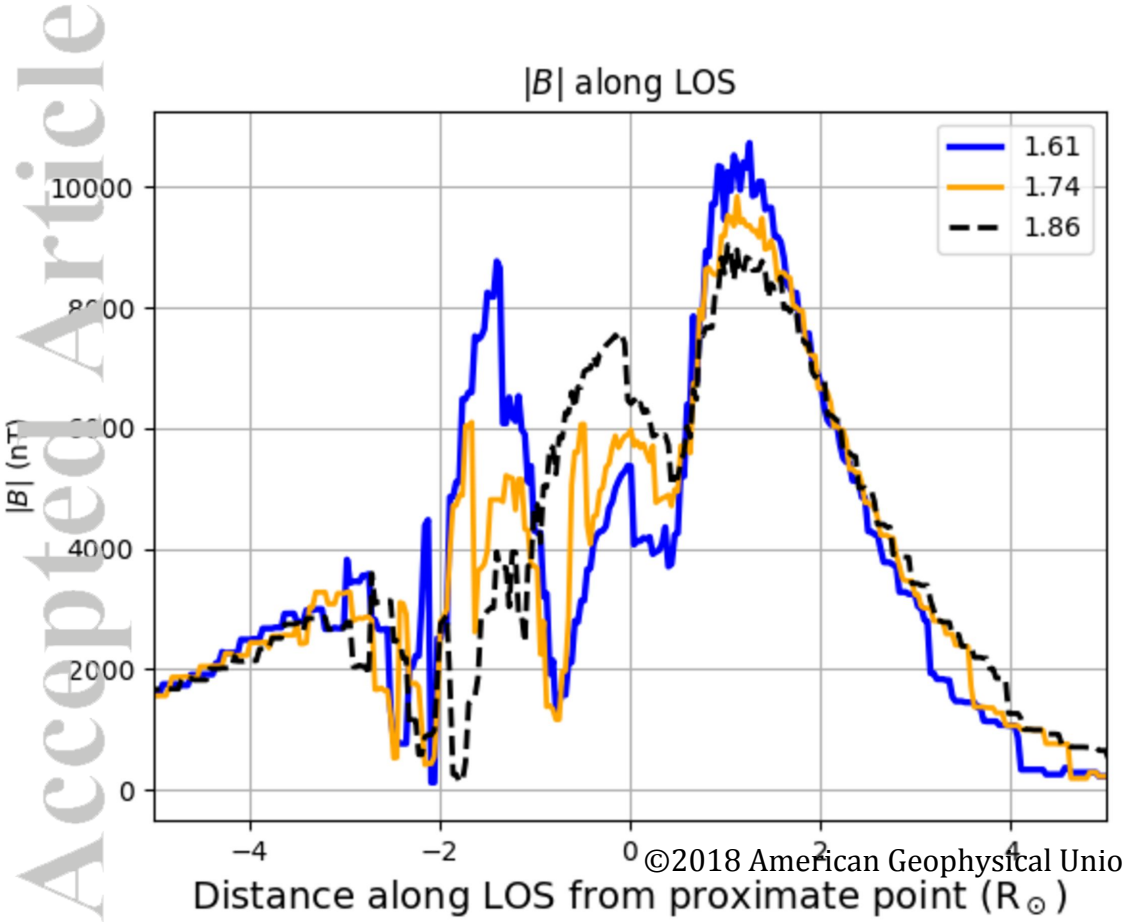

Figure 6.

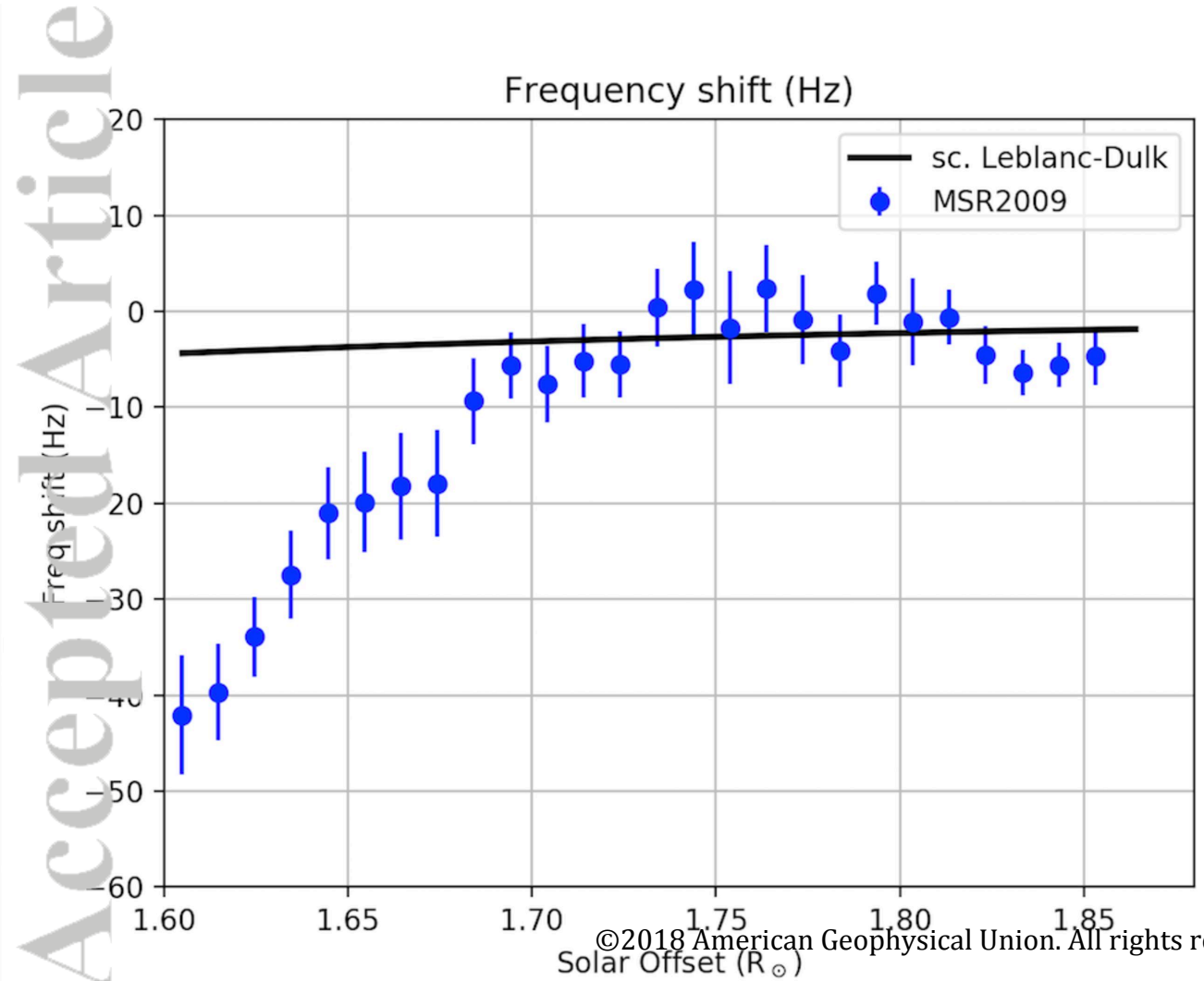

Figure 7.

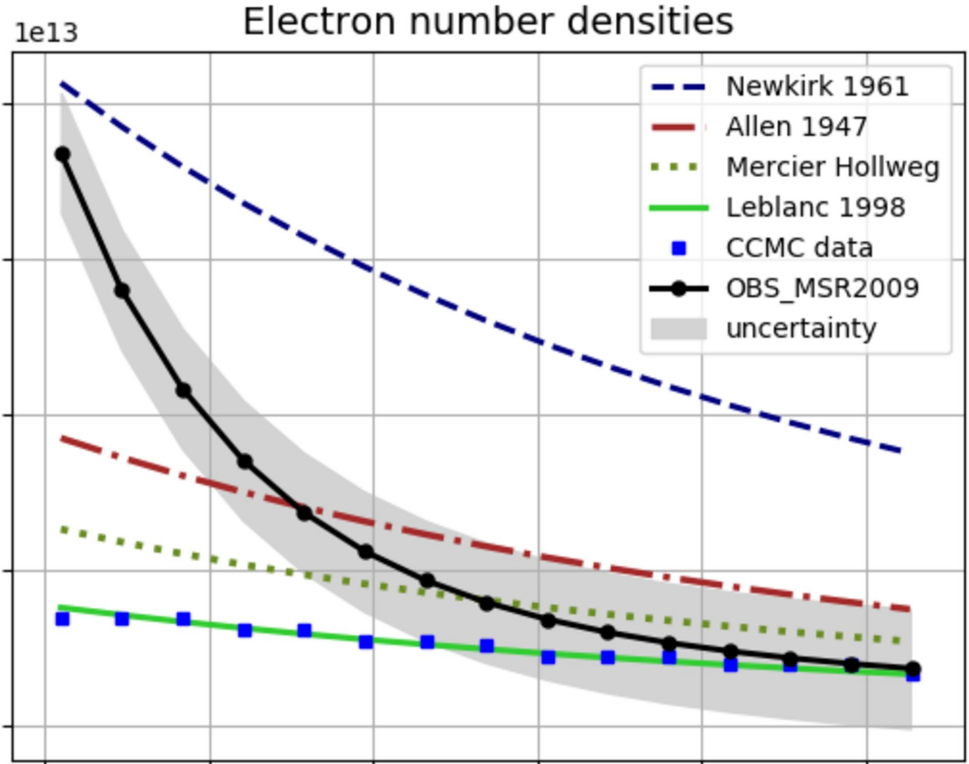

Figure 8.

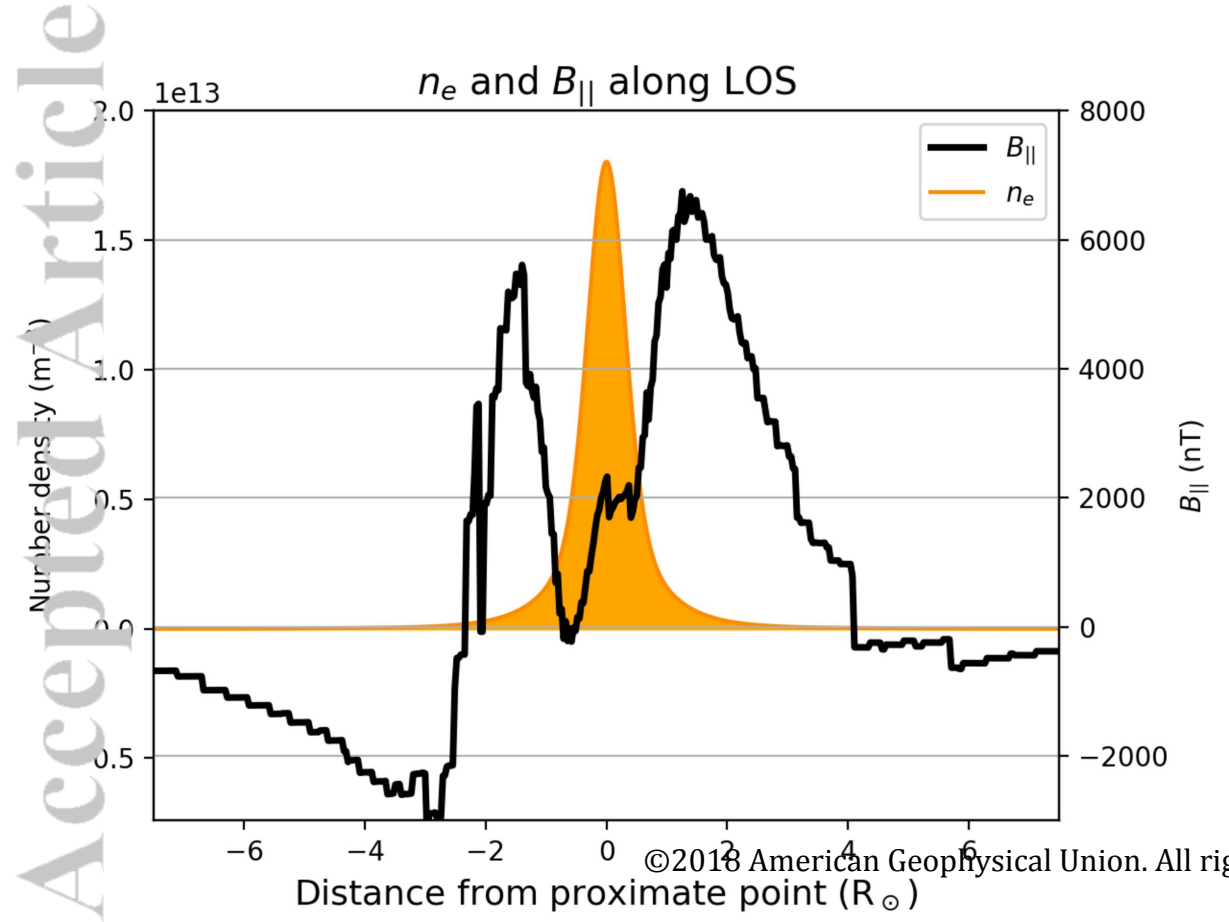

Figure 9.

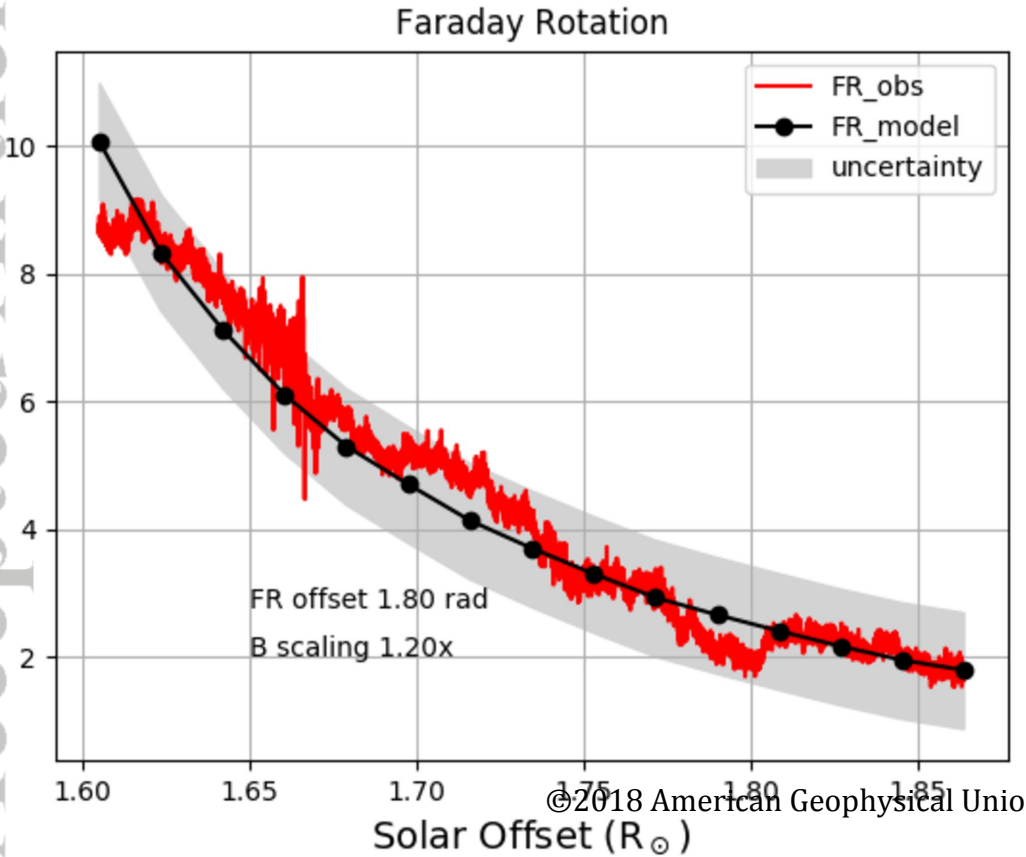

Figure 10.

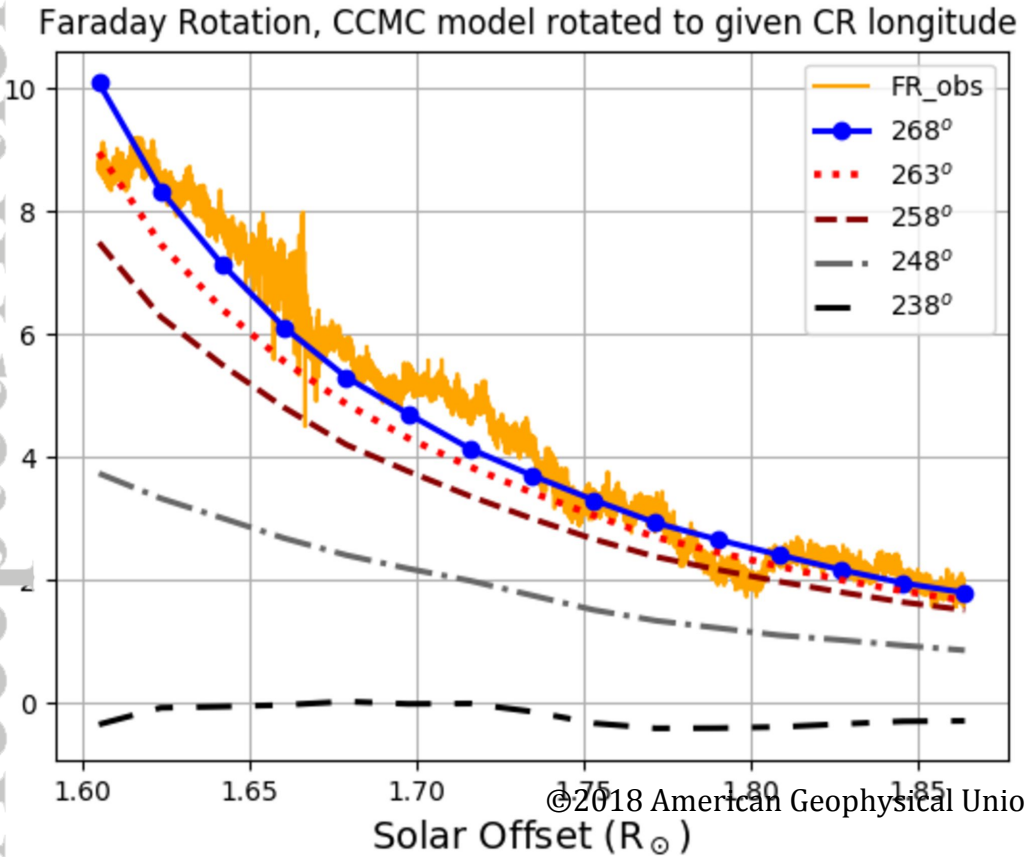

Figure 11.

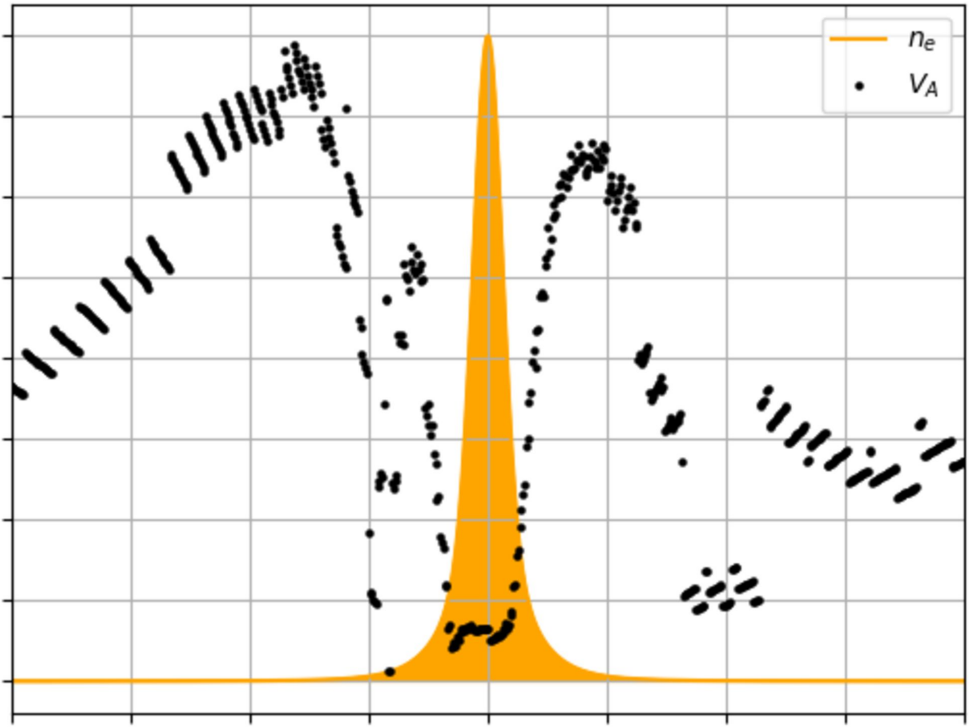

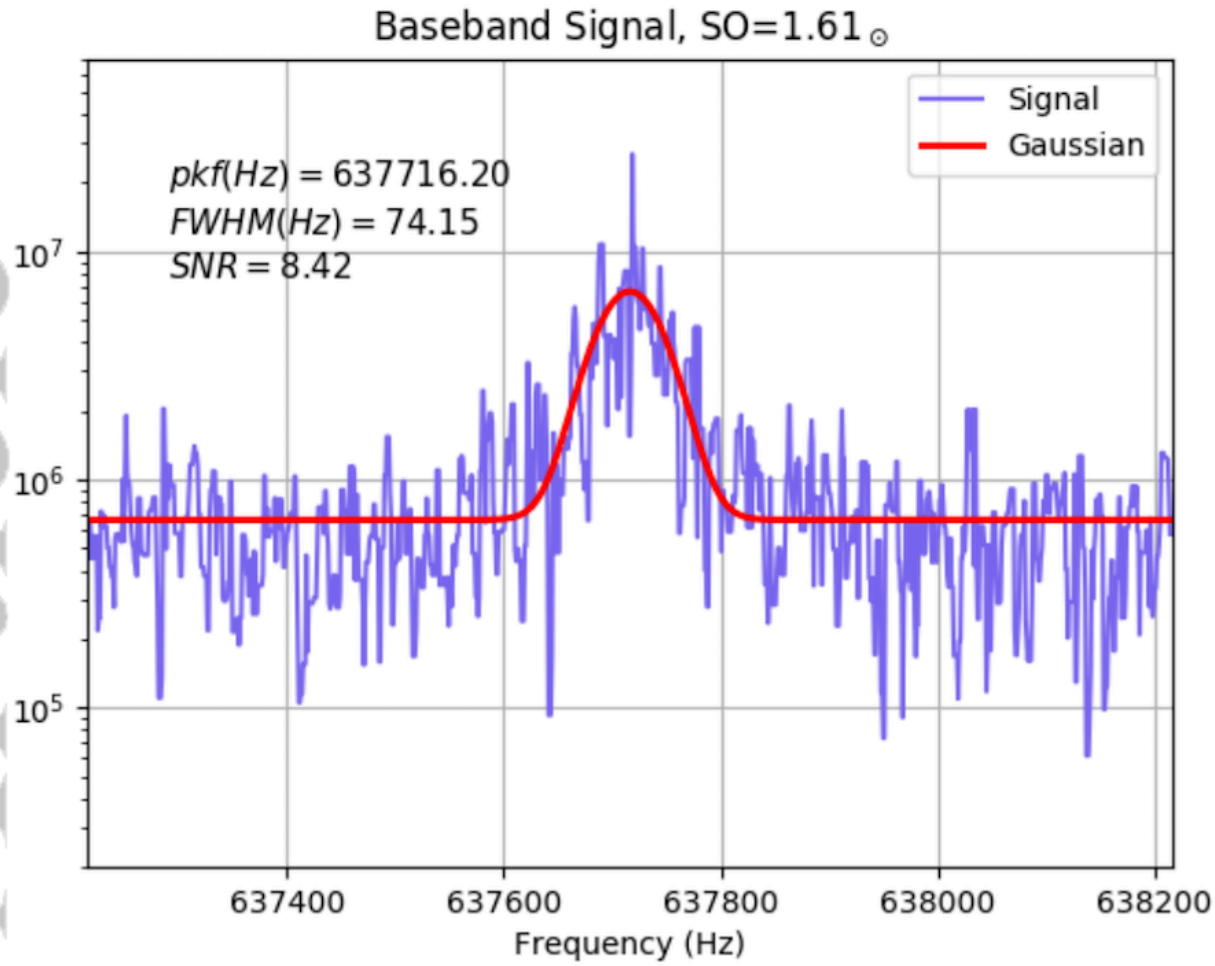

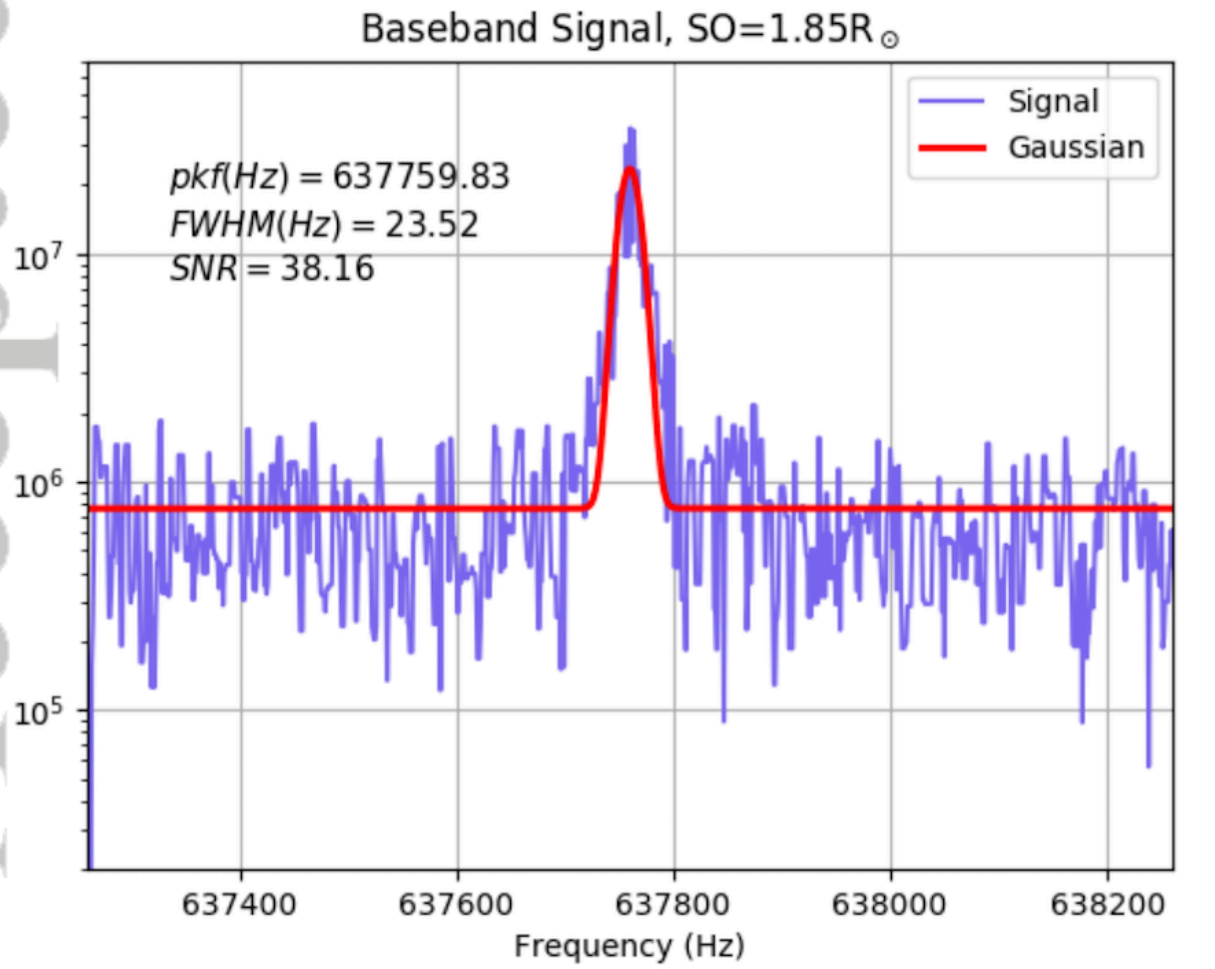

2019JA026937-f01-z-.png

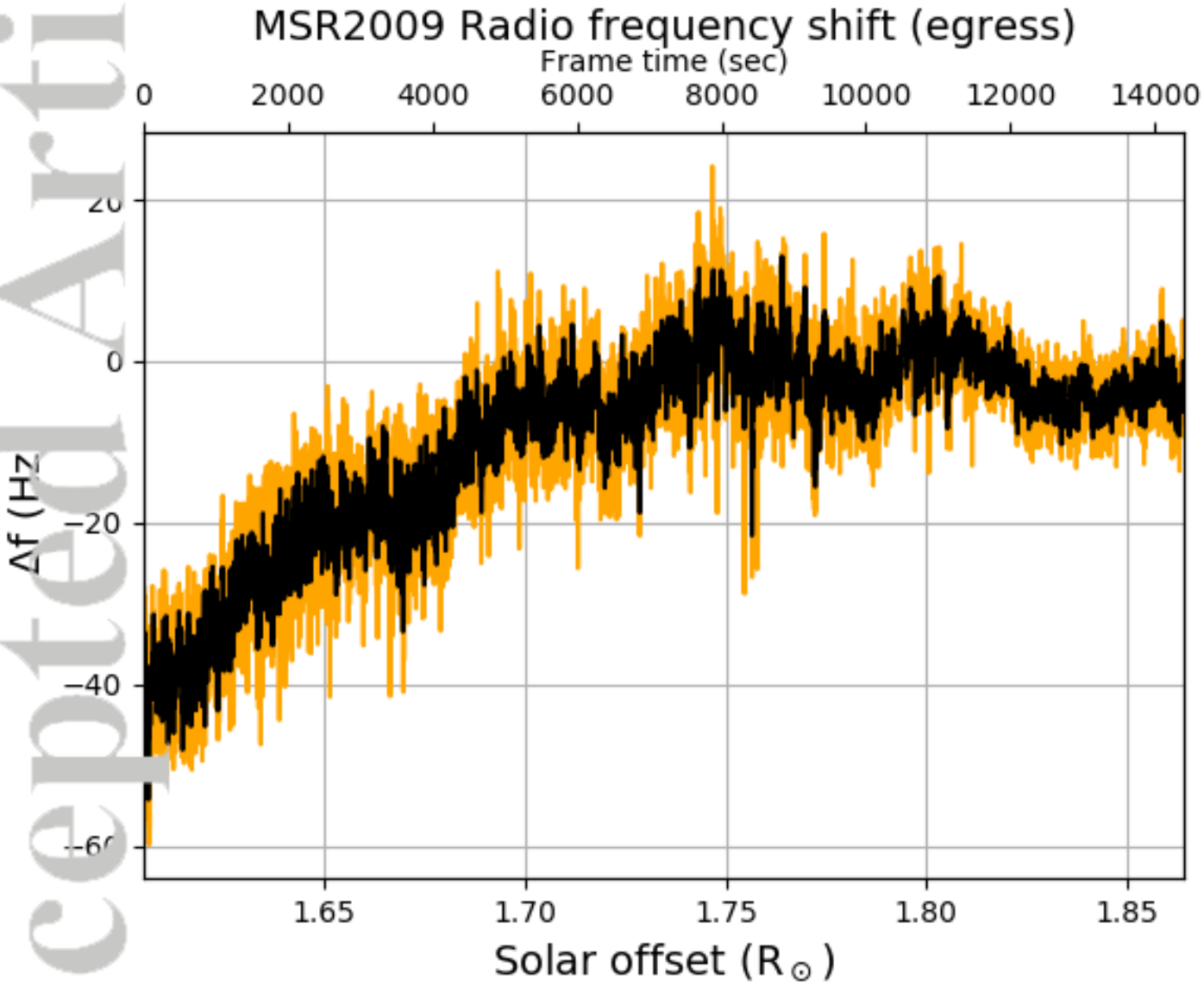

2019JA026937-f02-z-.png

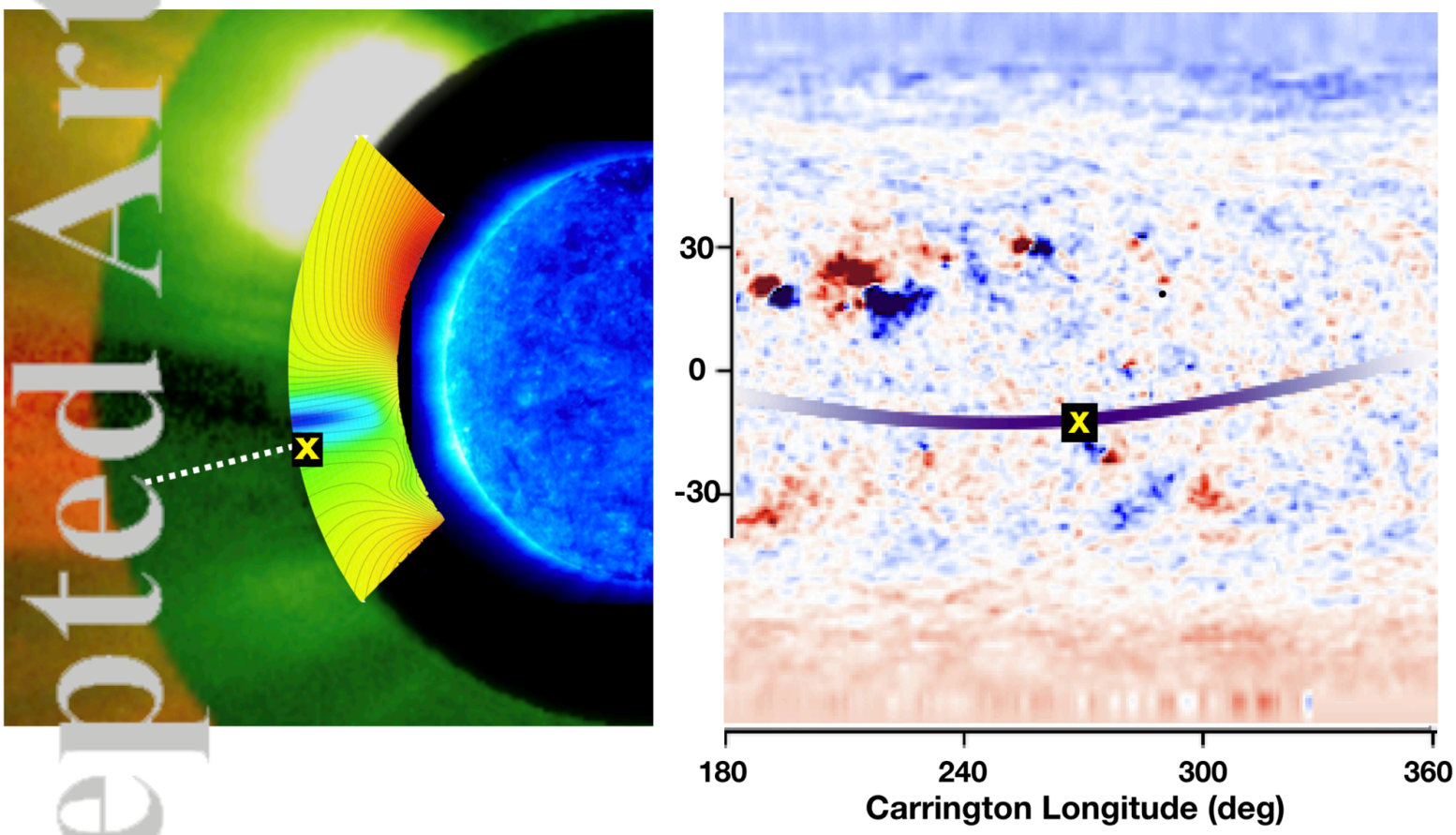

2019JA026937-f03-z-.png

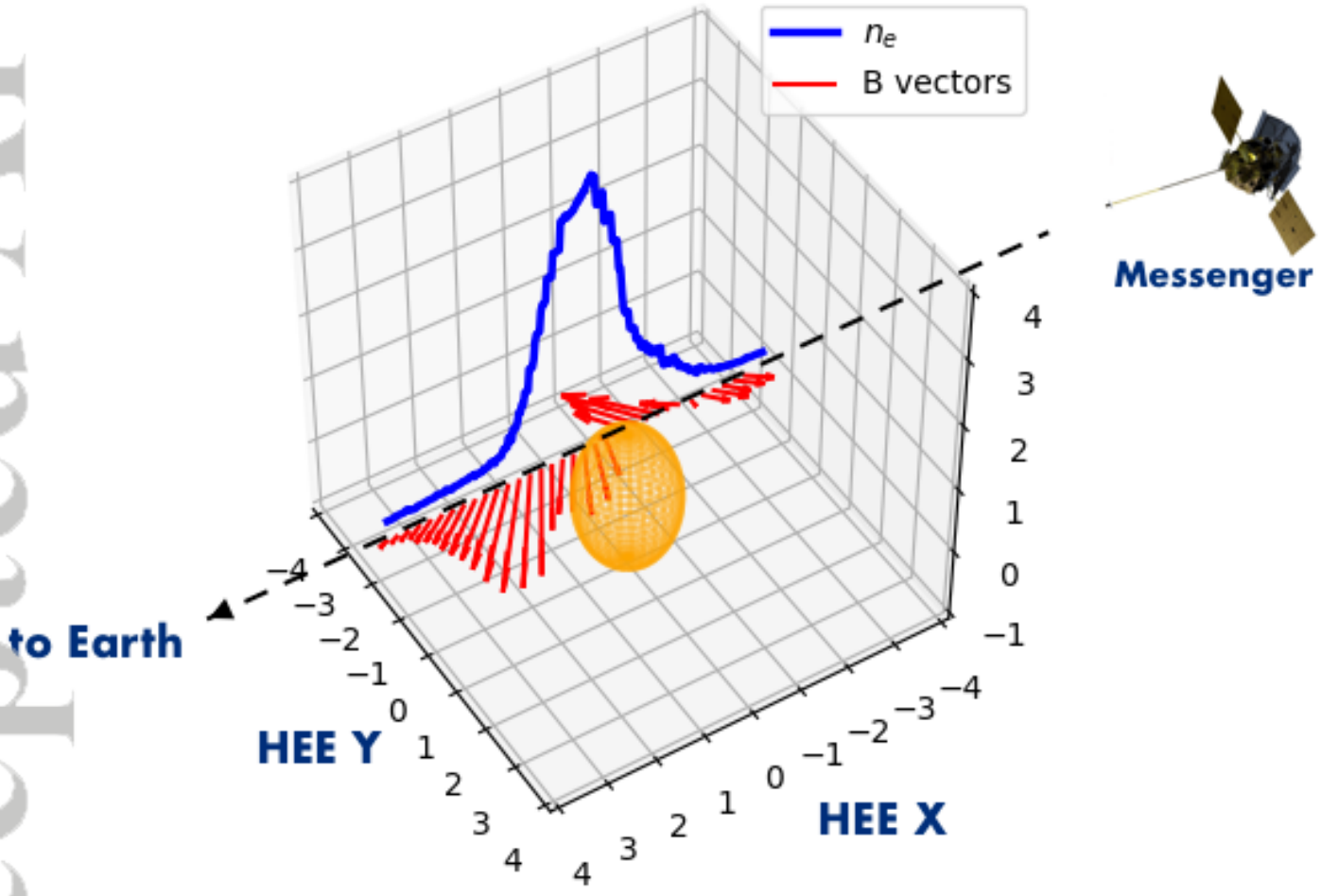

2019JA026937-f04-z-.png

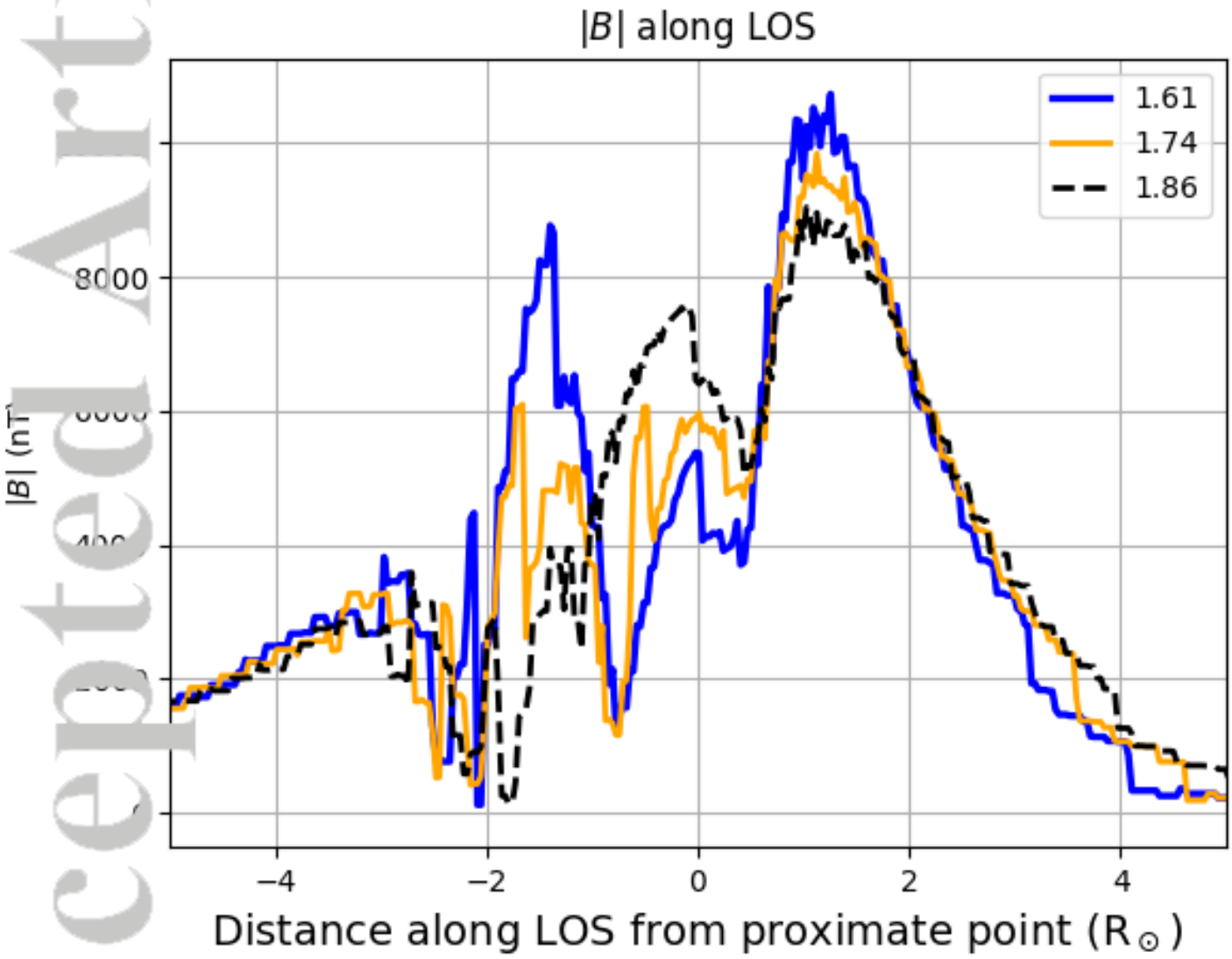

2019JA026937-f05-z-.png

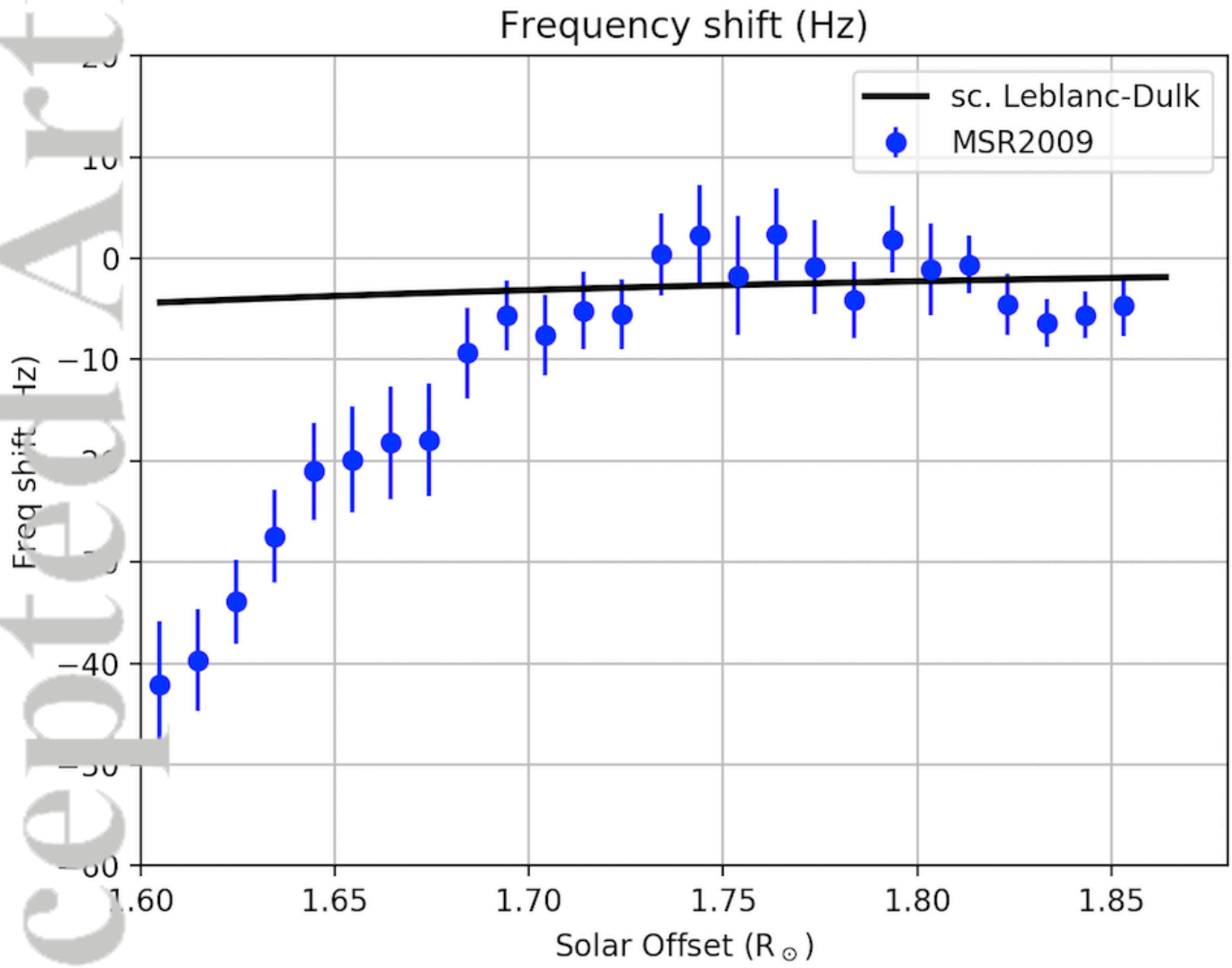

2019JA026937-f06-z-.png

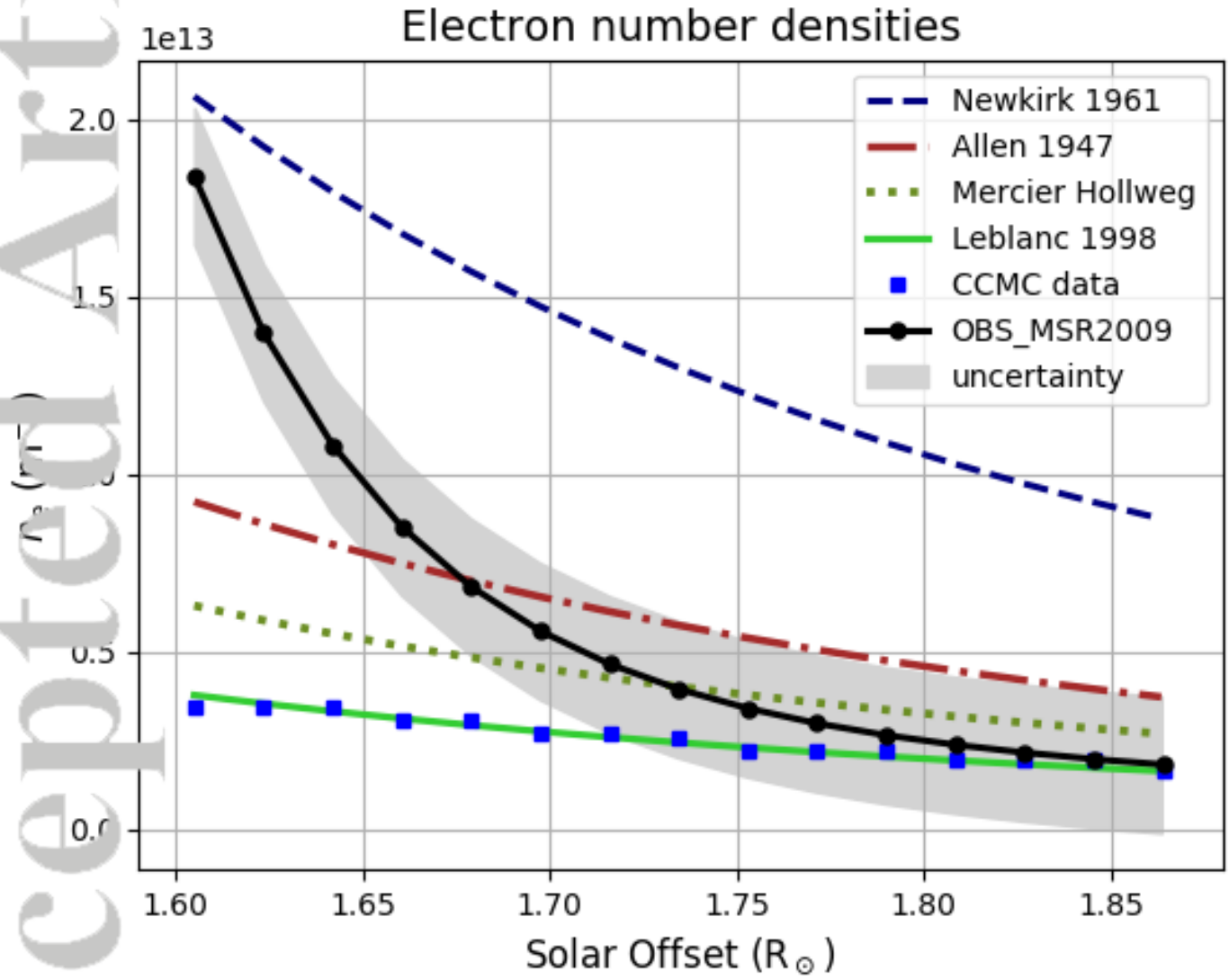

2019JA026937-f07-z-.png

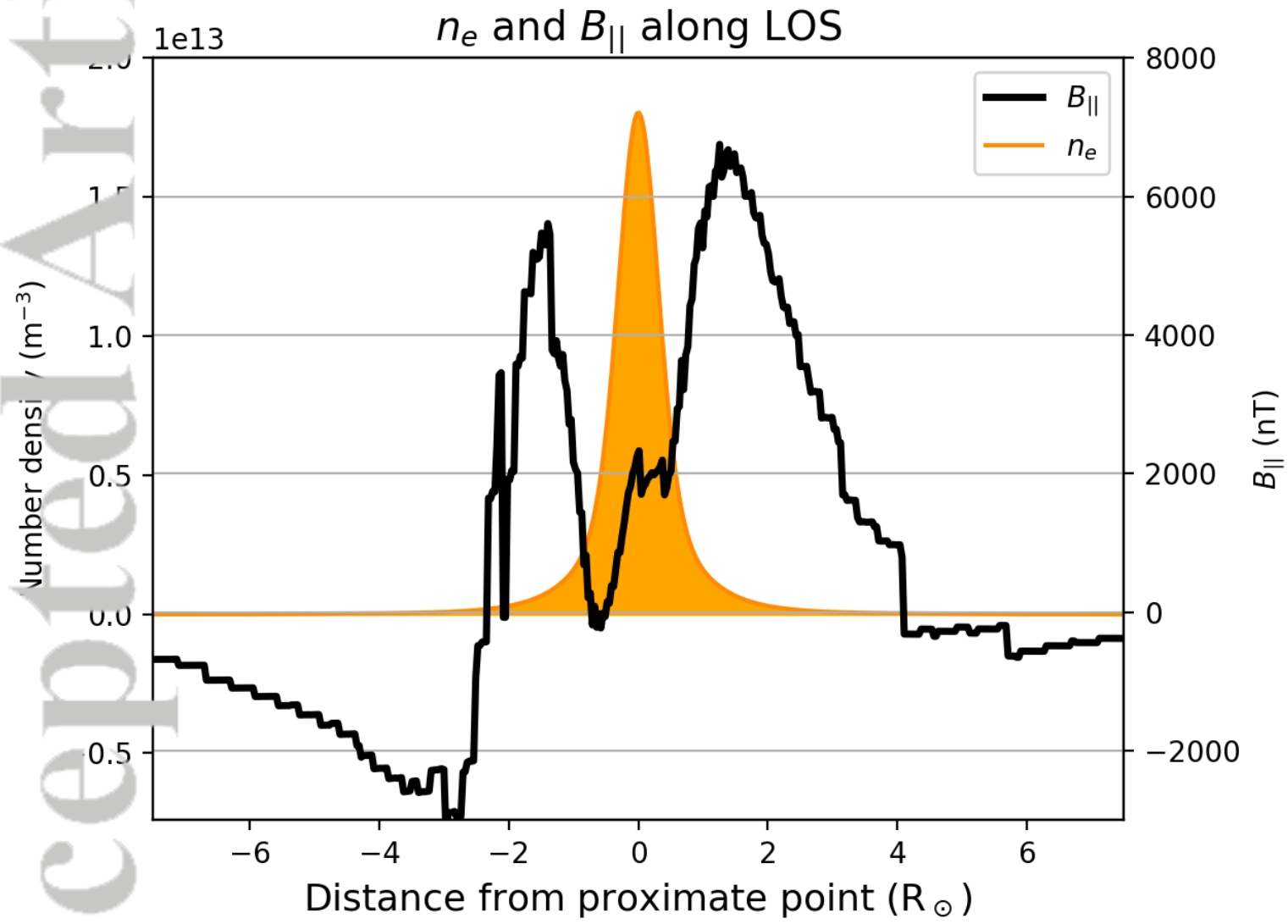

2019JA026937-f08-z-.png

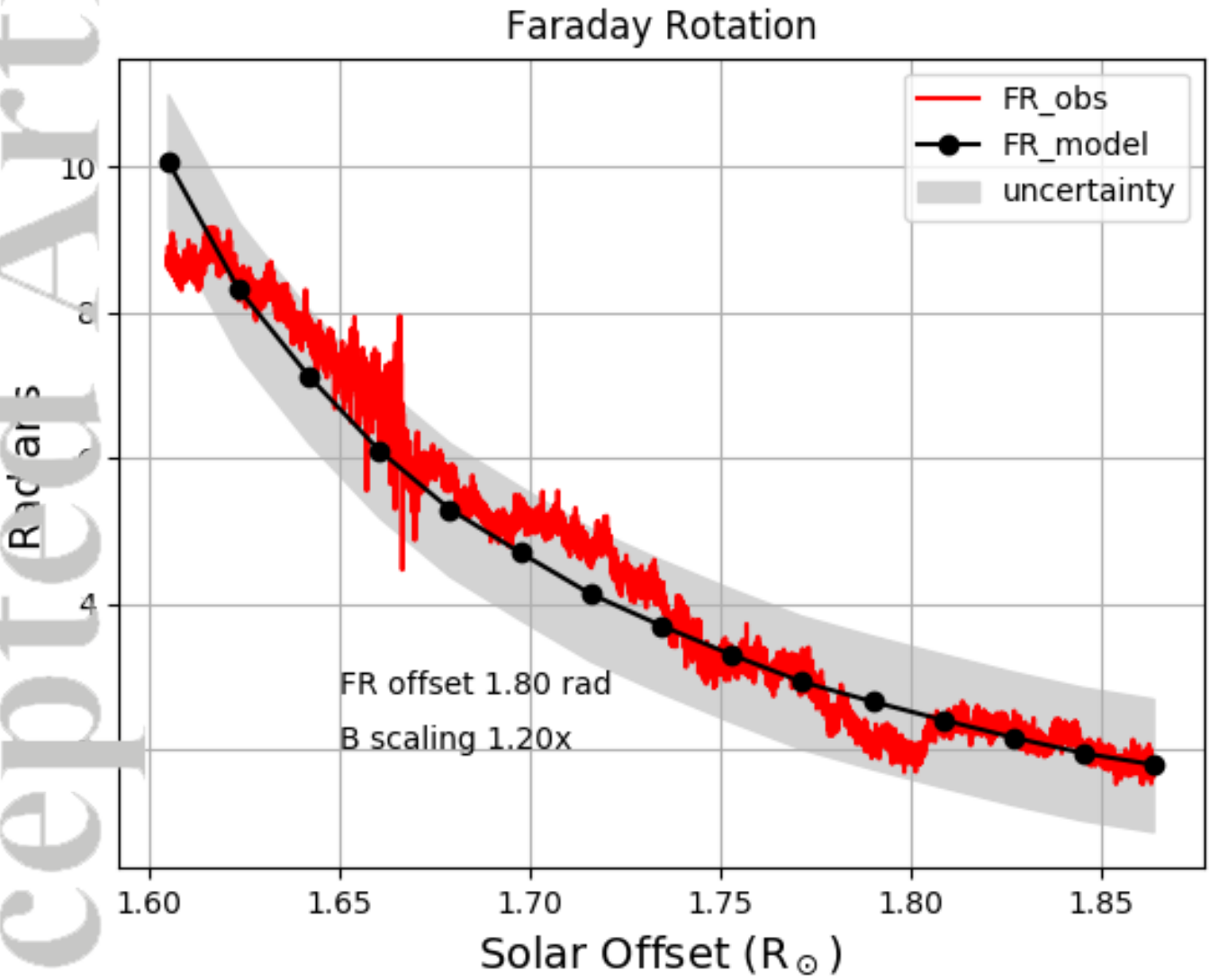

2019JA026937-f09-z-.png

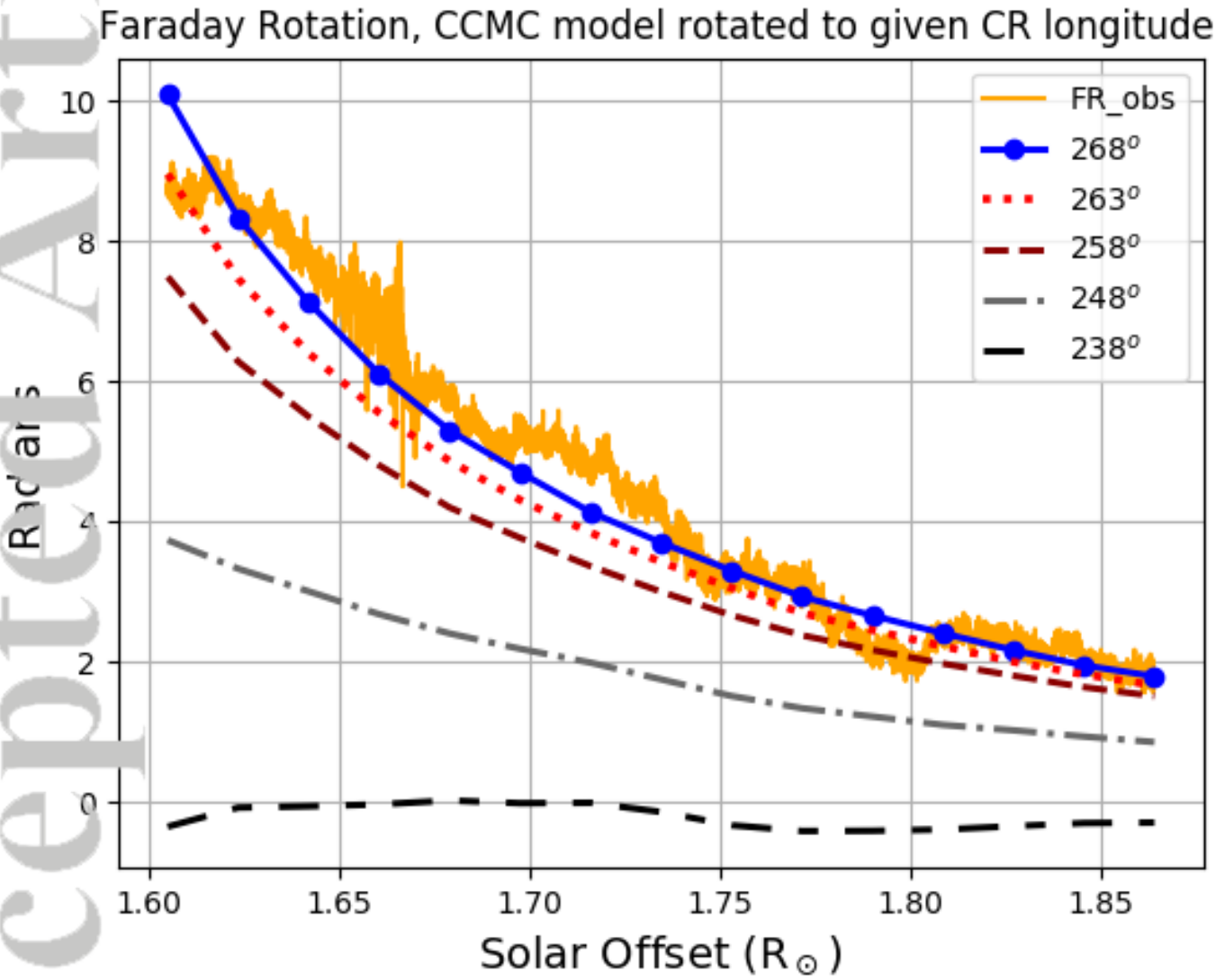

2019JA026937-f10-z-.png

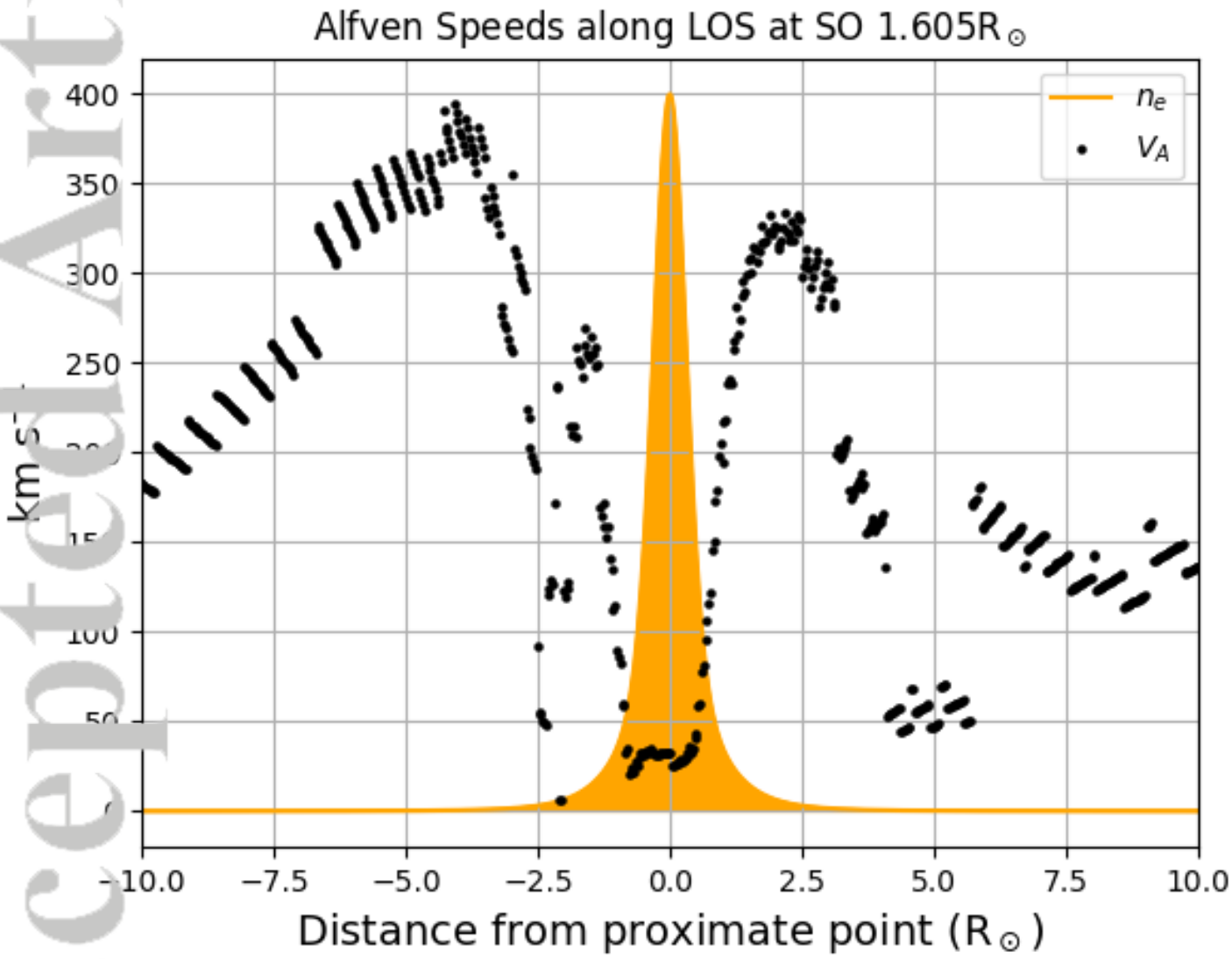

2019JA026937-f11-z-.png